A Split Hopkinson Pressure Bar Apparatus for High Strain Rate Testing of Interpenetrating Phase Composites (IPC): Measurements and Modeling

by

Chandru Periasamy

A thesis submitted to the Graduate Faculty of
Auburn University
in partial fulfillment of the
requirements for the Degree of
Master of Science

Auburn, Alabama
May 14, 2010

Keywords: structural foams, dynamic failure, interpenetrating phase composites, syntactic foam, split Hopkinson pressure bar, finite element analysis

Approved by

Hareesh V Tippur, Chair, Professor of Mechanical Engineering
Jeffrey C Suhling, Quina Distinguished Professor of Mechanical Engineering
James S Davidson, Associate Professor of Civil Engineering

Abstract

Novel materials with enhanced mechanical performance and multifunctionality are of interest to automotive, aerospace and marine industries alike. Designing materials with multiple thermo-mechanical attributes while satisfying lightweight constraint is rather challenging. This challenge becomes even greater when materials are to withstand elevated rates of loading. In this thesis, (*i*) a 3D Interpenetrating Phase Composite (IPC) made of Syntactic Foam (SF) in an open-cell aluminum scaffold is proposed for high-strain rate applications and (*ii*) a split-Hopkinson pressure bar apparatus is developed for characterizing low-impedance materials such as the SF and IPC materials at high-strain rates. The SF used for making IPC is prepared by dispersing hollow glass microballoons into an epoxy matrix. The resulting SF is a two phase composite on a microscopic scale and a lightweight homogeneous, isotropic material on a macro scale. The infusion of SF in its uncured state into the aluminum scaffold results in an IPC with a continuous 3D interpenetrating network throughout the material volume.

A split Hopkinson pressure bar has been developed and calibrated for carrying out high-strain rate stress-strain response measurements on low impedance materials. Dynamic compression characteristics, including strength and energy absorption features of IPC made of four different volume fractions of microballoons in SF are measured using this apparatus and compared. Measurements on pure SF counterparts are also carried out for evaluation relative to IPC. The results show that in general, the IPC foams

outperform the SF samples in terms of compressive strength and energy absorption per unit volume. The underlying deformation processes are evaluated optically using real-time high-speed photography as well as post-mortem analysis of deformed samples using scanning electron microscopy. The former includes the development of a novel grid-based method for measuring surface displacements and strains.

An idealized elasto-plastic unit cell finite element (FE) model based on explicit dynamics is proposed for studying IPC foams. The 3D geometry of the aluminum component in the cubic unit cell is modeled as a tetrakaidecahedron, a 14 sided polyhedron, also called the Kelvin cell. The SF constituent of the IPC is modeled as an occupant of the rest of the unit cell. The computational model incorporates infinite elements to represent the far-field regions surrounding the unit cell. The infinite elements help simulate stress wave dynamics of a sample undergoing deformation in a split Hopkinson pressure bar. The computations are successfully compared with measurements for all the four cases. The contour plots of von-Mises stress, equivalent plastic strain and displacements in the loading direction are analyzed at different strain levels. In addition, the kinetic and strain energy histories absorbed by SF and aluminum ligaments in the IPC are quantified.

Acknowledgments

Table of Contents

List of Tables

List of Figures

1   INTRODUCTION

1.1 Motivation

The continued human quest for making lives more comfortable has increased demands on engineering and technology. Lately, researchers have been looking towards nature for inspiration to meet some of these demands such as those involving materials and structures. The field of science and engineering which focuses on studying and researching bio-inspired materials and structures is called biomimetics [1]. Naturally occurring structural materials have undergone millions of years of evolutionary processes to adapt to the changing needs of their environment and functionality. So, it is only wise to adopt some of these examples in the process of developing new structural materials.

Recent advances in commercial and defense automotives, as well as marine construction, require innovative lightweight materials that could serve in the design of stiff and tough structures capable of absorbing impact energy. This concurrence of material properties cannot be easily formulated into a single material system. The microstructure of some naturally occurring materials such as bone (Fig 1.1) and nacre have a 3D interpenetrating structure [2], often made up of two or more biological phases. Thinking along these lines, and considering the combined requirement of structural integrity and energy absorption, an Interpenetrating Phase Composite (IPC) [3] made of two phases – one, brittle Syntactic Foam (SF) and the other, ductile aluminum (Al) foam

is being proposed in this thesis work. In general, IPCs are multiphase materials in which each constituent forms a continuous 3D network within the material volume. Thus, each phase in its stand alone state can be imagined to have an open-cellular microstructure.
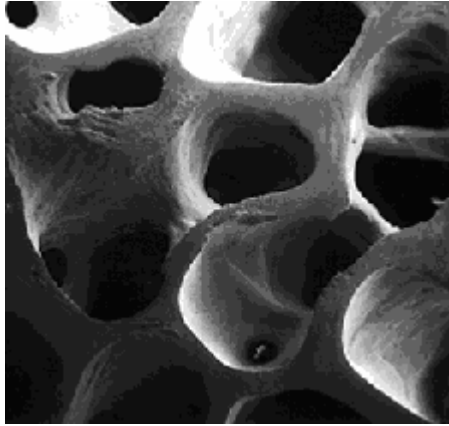
Figure 1.1: Cross section view of a human bone
(*From www.health.state.ny.us/diseases/conditions/osteoporosis/needknow.htm*)

Even though IPCs are heterogeneous on a micro/meso scale, the macro scale response is often isotropic. Each phase offers its own unique property to the IPC as a whole. For example, one phase might offer good toughness and thermal conductivity, while the other might enhance stiffness and dielectric properties. This co-existence of desirable properties without significant directional dependency or distinct weak planes (as opposed to conventional layered composites) makes an IPC attractive for structural applications. That is, each phase of an IPC contributes its unique property to the overall structural response synergistically. The above mentioned possibilities invite an indepth study on the IPC.

1.2 The syntactic foam / aluminum foam based IPC

In this work, the IPC is made of two phases – a polymer based Syntactic Foam (SF) and an open-cell aluminum (Al) foam. SF is a low density composite comprised of epoxy (or, any polymer) and hollow glass (or, any ceramic) microballoons. The microballoons are microscopic hollow spheres, usually a few micrometers to several hundred microns in diameter, and wall thickness ranging from fraction of a micron to a few microns. When these two materials are mechanically blended and cured, they form a two phase composite on a micro scale. Considering the size of the microballoons and their uniform distribution within the epoxy matrix, the resulting composite can be regarded as an isotropic material on a macro scale. The microballoons are hollow (with a partial pressure) which makes the syntactic foam lighter as well as buoyant. This unique combination of low density and buoyancy makes SF an ideal choice for marine applications (Fig. 1.2). Metal foams, on the other hand, are broadly classified into open-cell (Fig. 1.3(a)) and closed-cell (Fig. 1.3(b)) foams. They are typically used for energy absorption and heat dissipation applications. The closed-cell foams in particular are used as layers in sandwiched sheets for energy absorption. The open-cell foams, on the other hand, are also used for other applications [2] such as cryogenics, filteration, missile baffles, etc. Due to their relatively high cost, metal foams are only used in areas of advanced technology, such as aerospace structures.
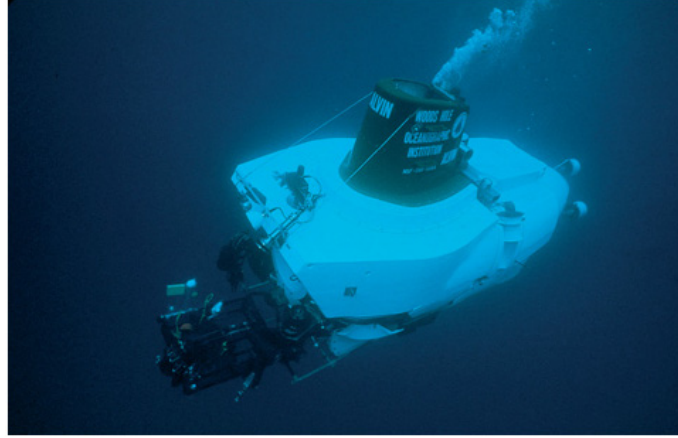
Figure 1.2: Syntactic foam used in submersible vehicles in marine environments

(From www.naval-technology.com)

(a)

(b)
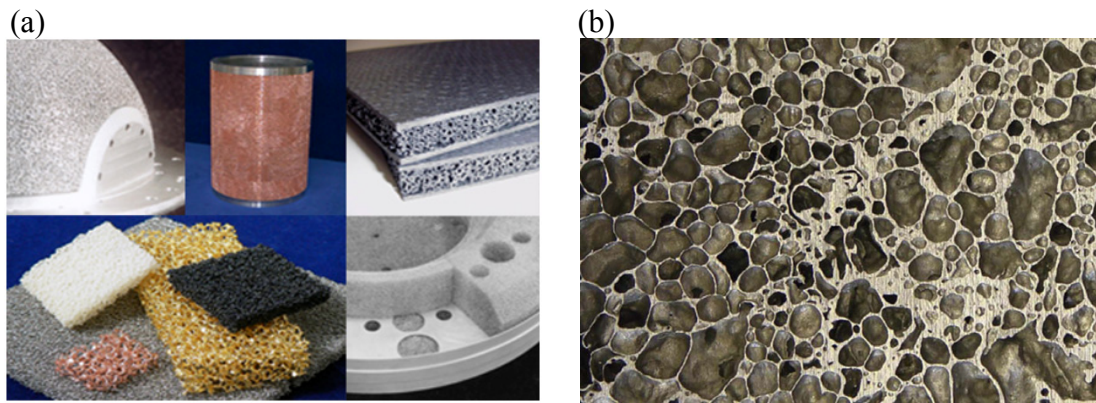
Figure 1.3: (a) Open-cell metal foams made of different materials (*from www.ergaerospace.com*); (b) Closed-cell aluminum alloy foam (*from Reference [4]*)

The IPC used in this work is made by infusing the SF into the open-cell aluminum foam. The term "Interpenetrating" signifies that each phase of the composite is continuous and forms a network of its own. Figure 1.4 shows a schematic of an interpenetrating network. The region shown in red (gray) represents one phase of the network, and the region shown in white is the second phase. (In reality, the empty space between the two phases is occupied by one of the two phases.) It can be seen that each

phase is three dimensionally continuous and also forms an interpenetrating network. A material of this type can prove to be advantageous in many applications as it can offer the combined properties of the two different materials synergistically. For example, in the SF / aluminum foam IPC, the aluminum foam might add to the stiffness of the whole structure, whereas the aluminum foam by itself does not have appreciable stiffness.
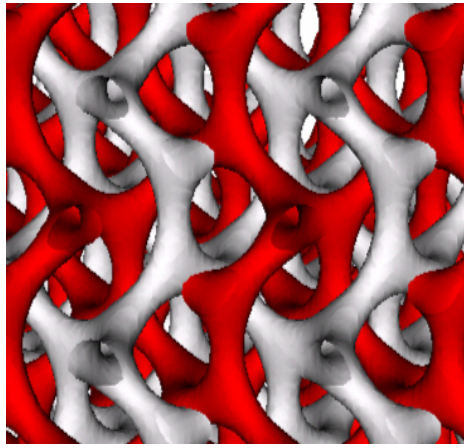
Figure 1.4: Schematic of a 3D interpenetrating network

1.3 Objectives

The following are the primary objectives of this work:

- Develop a split Hopkinson pressure bar (SHPB) set up for characterizing the compression behavior of low impedance materials and calibrate it for accuracy and repeatability of measurements.

- Prepare SF and IPC samples with different volume fractions (V_f) of microballoons in SF.

- Test dynamic compression properties, *viz*., stress-strain response, compressive strength and energy absorption of SF and IPC foams using the SHPB.

- Comparatively study the dynamic compression properties of SF and IPC and the effect of microballoon volume fraction V_f in the SF on the overall performance of IPC.

- Evaluate the high-strain rate performance of SF and IPC relative to the quasi-static counterparts.

- Perform high-speed photography and microstructural investigation of the deformed samples to understand the deformation processes in SF and IPC materials.

- Develop a finite element model of the IPC and simulate dynamic compression response using the measured mechanical responses of its constituents.

- Validate the computational model by comparing the computed high-strain rate IPC responses with the measurements.

1.4 Organization of the thesis

This thesis has been structured in such a way that the experimental aspects are presented first and then the computational work is detailed later on. The next chapter presents a literature review on (a) the Split Hopkinson Pressure Bar (SHPB) setup used for high-strain rate experimental characterization of materials and (b) the previous works on IPC. Chapter 3 describes material preparation methods for both SF and IPC foams. The experimental procedure and the evaluation of the SHPB apparatus, respectively, are presented in Chapters 4 and 5. The results of the experiments are detailed and analyzed in Chapter 6. For the purpose of comparison of the strain rate effects, the appropriated quasi-static results from a previous work [2] are also presented intermittently throughout this chapter. Chapter 7 presents the finite element procedure, including details on

geometric modeling, relevant material properties, model discretization and application of boundary conditions. A comparison of the experimental and computational results is also presented in this chapter. Finally, Chapter 8 summarizes the results of this work.

2   LITERATURE REVIEW

2.1 Split Hopkinson Pressure Bar (SHPB)

A split Hopkinson pressure bar is a device used to study the mechanical behavior of a material at high-strain rates. The principle behind the SHPB was first introduced by Bertram Hopkinson [5] in 1914. Hopkinson used the principle to measure the pressure developed in a bar when a blast occurs at one end of it. In his set up (Fig. 2.1), a bar was suspended with one end attached to a detonation mechanism and the other end in magnetic contact with a time piece. When a blast occurs at one end, a pressure pulse travels through the suspended bar and impacts the time-piece. At the free end of the time piece, the pressure pulse reflects back as a tensile pulse, and when it reaches the time piece – bar interface, the time piece separates from the bar and flies into a momentum trapping mechanism. The energy recorded by the momentum trap corresponds to the energy of twice the wave length of the pressure pulse in the time piece.

Subsequently, Hopkinson's principle was used by Robertson [6] in 1921 and by Landon and Quinney [7] in 1923. The technique was then modified in 1948 by Davies [8] who used condensers for measuring displacements in the pressure bar. In 1949, Kolsky [9] modified the setup further by adding a second pressure bar and placed the specimen between the two bars. He used a cylindrical condenser microphone to measure the amplitude of the pressure pulse produced by firing a detonator at the free end of the

incident bar. At the free end of the second bar, he used a parallel plate condenser microphone to measure displacement. He used the signals from the two condensers to measure the stress-strain response of the specimen. Most recently, researchers have replaced the detonator with a striker impacting the incident bar (at a known velocity) and the condensers with strain gages pasted on the pressure bars.
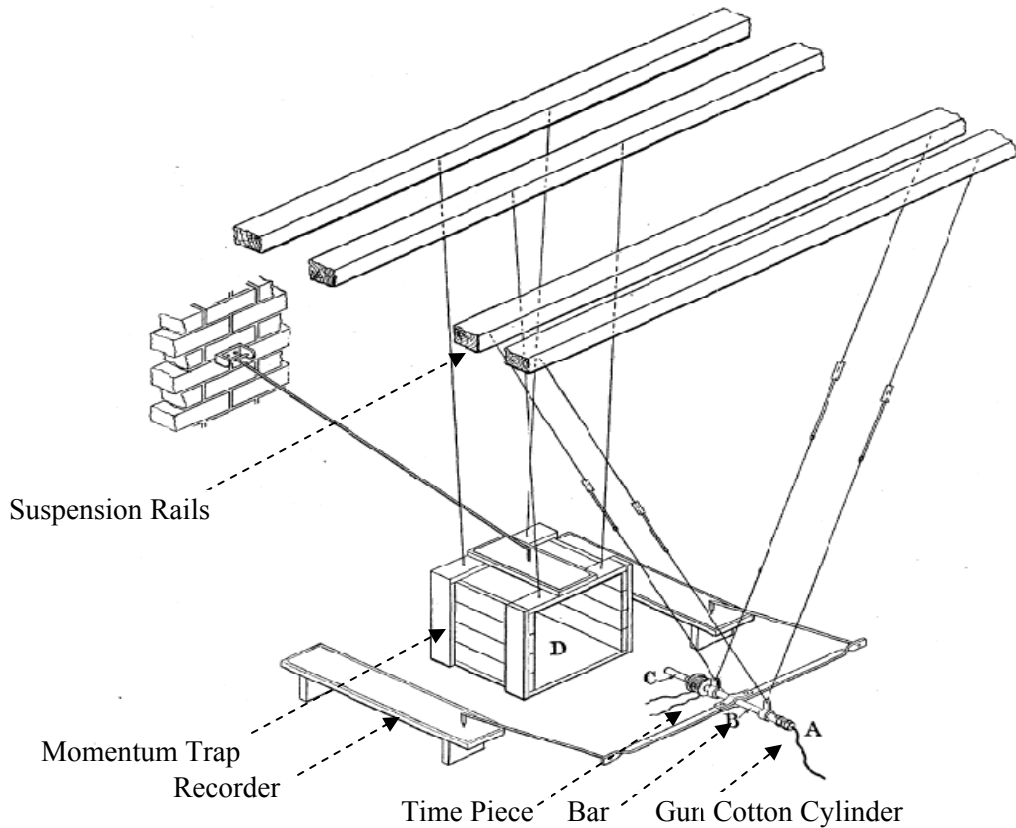
Figure 2.1: Hopkinson's Setup

(Reproduced from reference [5])

The invention of the split Hopkinson bar has helped researchers to dynamically test a variety of solids including metals, polymers, ceramics and composites [10]. Modifications to the conventional Kolsky bar have been made by many researchers to

test brittle materials [11, 12], low-impedance or soft materials [13, 14, 15] and structural foams [16]. To test low-impedance materials at high strain rates, Chen *et al*. [13] used a hollow high-strength aluminum alloy for the bar material in place of the conventionally used solid circular cross sectioned steel bars. It has been reported in the same work that the reduced cross sectional area of the hollow aluminum bars increased the amplitude of the transmitted strain signal in the bars by an order of magnitude. Song and Chen [16] obtained the dynamic compressive response of epoxy syntactic foam using a SHPB setup in which they used an annealed copper pulse shaper at the striker-incident bar interface. In their work, it has been demonstrated that the specimens were under dynamic stress equilibrium during loading due to the effect of the pulse shaper. Recently, Subhash and Liu [17] tested an epoxy-based polymeric foam for its crushability under rigid lateral confinement. In their work, they used magnesium bars to test samples under low stress, and steel bars for samples under high stress. Thus, it is evident that material properties (density in particular) play a significant role in the stress wave history in the bars. Likewise, Bouix, *et al*. [18] used nylon bars in their SHPB setup to dynamically characterize the compression properties of polypropylene foams. It is to be noted that nylon which is visco-elastic, was the choice material for testing a low impedance rubbery material.

2.2 Previous works on IPC

The primary material system under investigation in this work is an IPC, which is a two phase composite. The following is a review of some of the works on different IPC systems available in the literature. Among the existing works on IPCs, Prielipp *et al*. [19]

studied the mechanical properties of aluminum/alumina interpenetrating composite and measured fracture strength and fracture toughness of the composite as a function of ligament diameter and volume fraction of the metal reinforcement. The metal reinforced interpenetrating composites consistently had higher fracture strength. Breslin *et al.* [20] characterized an aluminum/alumina IPC obtained using the liquid phase displacement reaction method. The resulting IPC showed enhanced density, thermal conductivity and CTE characteristics, without compromising stiffness or fracture toughness. Travitzky *et al.* [21] showed that the residual stresses developed in silicon during solidification of molten Si within an Al_2O_3 matrix results in the greater strength and fracture toughness of the resulting Al_2O_3/Si interpenetrating system. Wegner and Gibson [22] developed finite element models to predict the elastic, strength and thermal expansion properties of two phase IPCs. They attributed the enhancement in the thermo-mechanical properties to the contiguity of the phase with the most desirable property. In a later work [23], the same authors studied the mechanical behavior of resin-impregnated porous stainless steel. The yield strength, ultimate strength, elongation at failure and the elastic modulus were all found to increase with an increasing volume fraction of steel. Skirl *et al.* [24] examined the thermal expansion behavior of alumina/aluminum IPC. A pressure infiltration technique was used to introduce aluminum into slip cast and then sintered alumina. The tensile and compressive residual stresses in alumina and aluminum phases were found to enhance the overall thermal coefficient of expansion. An increase in failure strain with increased metal content was also reported. Mayer and Papakyriacou [25] studied the fatigue behavior of graphite/aluminum IPC. The lightweight metals, such as aluminum, were infiltrated into polycrystalline graphite to improve the fracture toughness of

polycrystalline graphite. A 30% increase in the cyclic strength and a 10% increase in the endurance limit were also reported. Tilbrook *et al*. [26] measured the effective mechanical properties of alumina-epoxy interpenetrating composites and reported strong dependence of properties on the composition and the processing of the material itself. Etter *et al*. [27] examined the flexural strength and fracture toughness of graphite/aluminum IPC at room temperature and at 300^oC. A 200% improvement in both these characteristics for IPC over un-infiltrated material at room temperature was reported. Additionally, no significant drop in properties was seen at elevated temperatures. Jhaver and Tippur [28] demonstrated the feasibility of a lightweight IPC foam by infiltrating a syntactic foam (SF) [29-31] into an open-cell aluminum network and examining quasi-static uniaxial compression response experimentally and numerically. They showed that the compressive strengths and energy absorption capacities of IPC samples were greater than those of the corresponding syntactic foam samples.

As noted in the above reports, the enhancements in the effective mechanical properties of IPC are dictated by the contiguity of the phase with the most desirable properties. An IPC foam formed by a continuous interpenetrating 3D network of syntactic and aluminum foams has the potential for improving structural integrity with good energy absorption characteristics, thus making it a worthwhile material system for further study. This work builds on the feasibility study of the IPC foam first reported in Ref. [28].

3   MATERIAL PREPARATION AND SAMPLE DIMENSIONS

This chapter details the preparation of the IPC foam material and the choice of dimensions of the samples. In the first section, the sequential procedure adopted for the preparation of the SF samples is described, followed by a description of the preparation of the IPC samples. Later, a microscopic view of an IPC sample cross section is discussed with regard to the bonding between SF and aluminum and the randomness of the microballoon distribution. Lastly, a discussion on the sample dimensions and the reason for choosing those dimensions will be presented.

3.1 Material preparation

The constituents used for preparing the SF foam were a low viscosity epoxy (Epo-Thin^{TM} from Beuhler, Inc. USA, mass density of the resin ~1100 kg/m^3) and hollow glass microballoons (K-1^{TM} microballoons from 3M Corp., bulk density 125 kg/m^3) of average diameter of ~60 μm and wall thickness of ~0.6. Syntactic foam samples were prepared by mixing the desired quantity of microballoons into epoxy resin. The uncured syntactic foam was then transferred into a silicone rubber mold (Fig. 3.1 (a)) after vacuuming (at approximately -75 kPa gage pressure) to remove any trapped air bubbles in the mixture. The mixture was then allowed to cure for at least seven days before being removed from the mold and machined to size as shown in Fig. 3.1 (c).

13
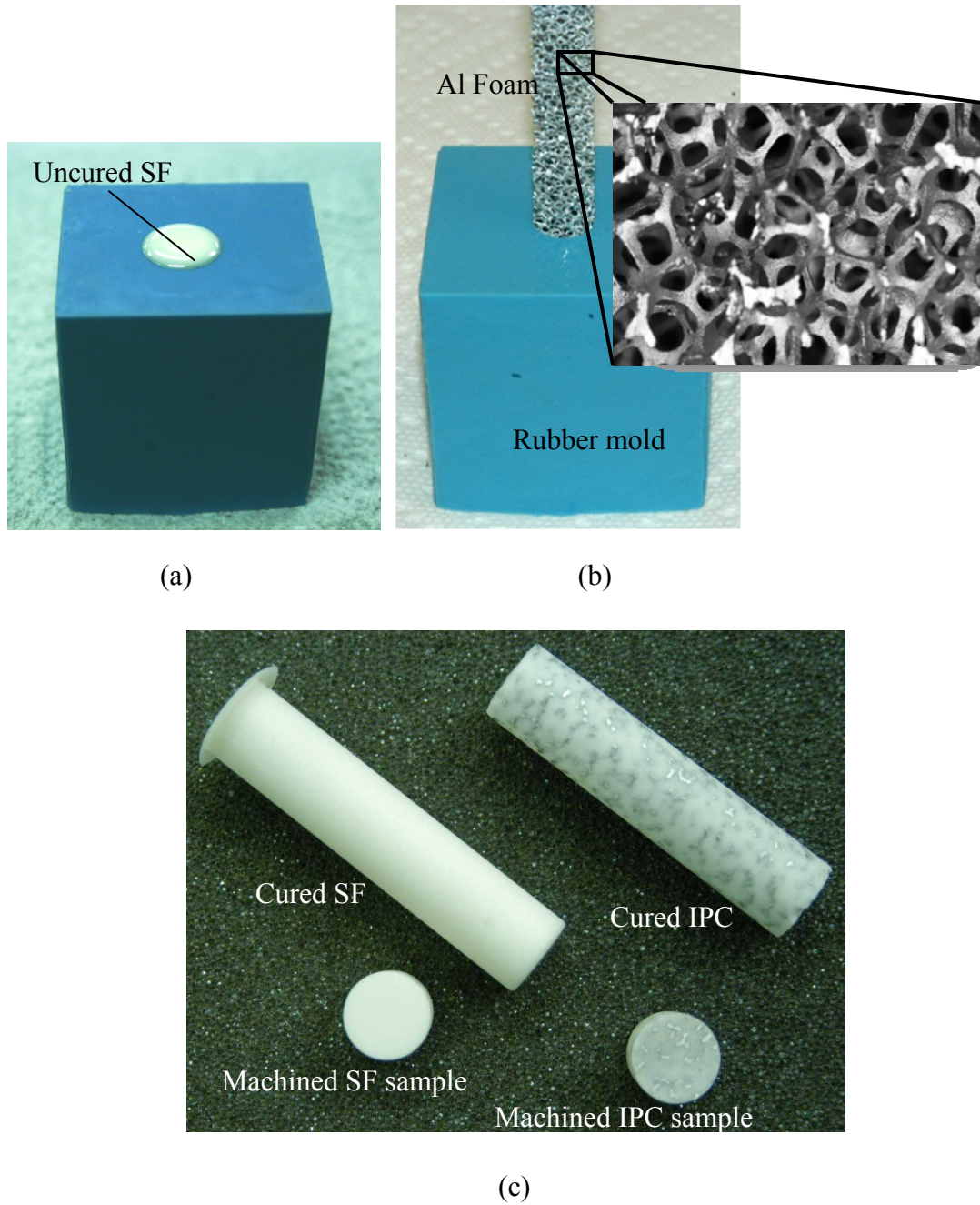
Figure 3.1: (a) Rubber mold with uncured SF, (b) Aluminum foam inserted into mold containing uncured SF, (c) Cast and machined SF and IPC samples

The metal foam used in the IPC was a commercially available open-cell Duocel® aluminum (Al 6101-T6) preform obtained from ERG Aerospace Corp., with a pore density of 40 pores per inch (~8% relative density). The metal foam was cleaned with

acetone and then coated with silane, γ-aminopropyltrimethoxysilane ($H_2NC_2H_4NHC_3H_6Si(OCH_3)_3$), to enhance the bond strength between aluminum ligaments and syntactic foam. To prepare the IPC, the degassed, uncured SF was prepared the same way as before. Then, the silane coated aluminum foam was slowly inserted into the mold (as shown in Fig. 3.1 (b)) containing uncured syntactic foam so that the syntactic foam filled the open-pores of the aluminum network. After curing for at least seven days, the unfinished sample was removed from the mold for machining (Fig. 3.1 (c)).
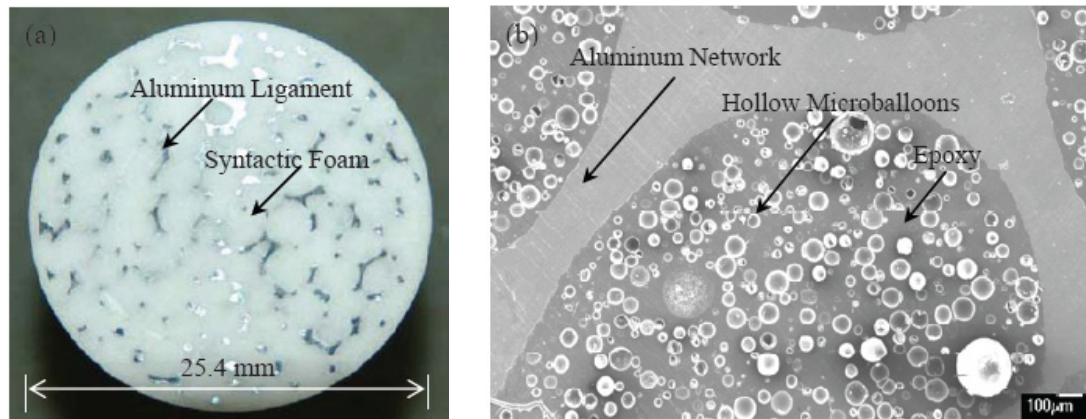
Figure 3.2: (a) Cross-section of IPC foam with 30% volume fraction of SF,

(b) SEM micrograph of IPC; (*From Ref. [28]*)

A photograph of the cross-section of the cured IPC foam is shown in Fig. 3.2(a). The shiny metallic ligaments of the aluminum preform interspersed within the syntactic foam can be readily observed. Figure 3.2(b) shows a micrograph of the cross section of the IPC with 30% microballoon volume fraction in SF. The interface between aluminum ligaments and syntactic foam is well defined without voids or cracks suggesting a good bond between the two phases. The microballoons also appear to be uniformly distributed within the epoxy matrix.

3.2 Sample dimensions

The cured SF and IPC samples were removed from the mold and rested for about a week before machining. The sample dimensions were determined based on a previous work by Gibson [32]. Gibson has analyzed size effects on foam test specimens, and proposed a specimen thickness (length) to cell size ratio (t/d) of 8 or above, so that the specimen better represents the bulk. By size effects, Gibson means the effect on the measured material properties when the macroscopic sample dimensions are of the order of the pore size. The aluminum foam used in this thesis work has a pore density of 40 pores per inch with 22 – 26 cells per inch according to the manufacturer. Therefore, it can be assumed that there are approximately 24 cells per inch on an average (Figure 3.3(a) shows the relative sizes of pores and cells). Thus, the individual cell size is approximately 1.06 mm (0.042 in). A t/d ratio of 9 was chosen for the SHPB tests. Accordingly, the samples used in the dynamic testing had a length of 9.5 mm (0.375 in) and a diameter of 12.7 mm (0.5 in) as shown in Fig. 3.3(b).

(a)   (b)
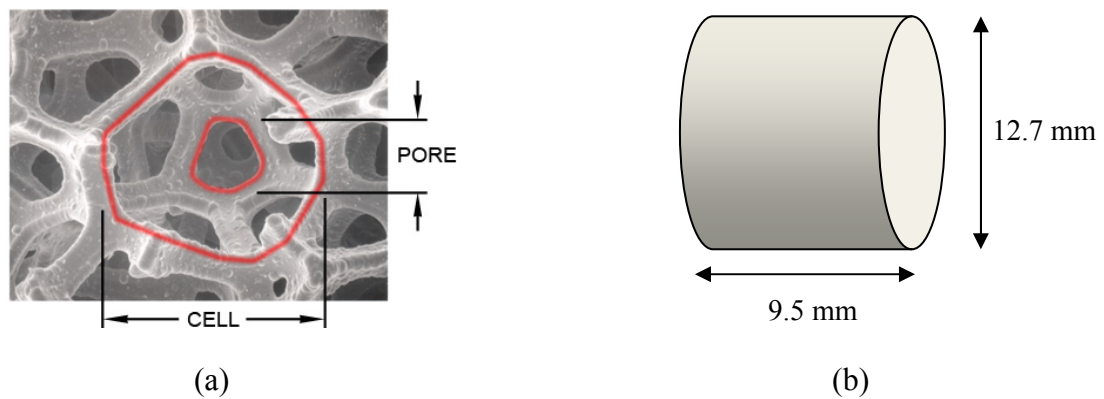
Figure 3.3: (a) Representation of pores and cells (*From www.ergaerospace.com*);

(b) Sample dimensions

From the dimensions shown in Fig. 3.3(b), the thickness (t) to diameter (D) ratio (or, slenderness ratio S_0) is 0.75. This S_0 was chosen with reference to the work published by Malinowski and Klepczko [33] in which they suggested an optimum value for use in SHPB tests for different material categories based on the axial inertia and interfacial friction of the sample material. According to their work, samples made of low flow stress materials such as gold and uranium should have $0.1 \leq S_0 \leq 0.5$. For samples made of moderate density metals like aluminum and copper they suggest an optimum S_0 range of 0.5 to 1.0, and for hard materials like high strength steels, an optimum S_0 range of 1.0 to 1.5. The IPC used in this work consists of aluminum and SF, which are made of moderately dense and brittle, but not hard materials. Logically, the integrated effect of combining the two materials in the IPC suggests a S_0 in the 0.5 to 1.0 range for the SHPB test samples.

4 EXPERIMENTAL PROCEDURE

The dynamic experiments were performed using a Split Hopkinson Pressure Bar [9] (SHPB) apparatus (Fig. 4.1) developed for this study. This chapter provides a detailed description of the experimental setup, the working principle and the theoretical basis for obtaining the dynamic stress-strain response of SF and IPC samples.

(a)
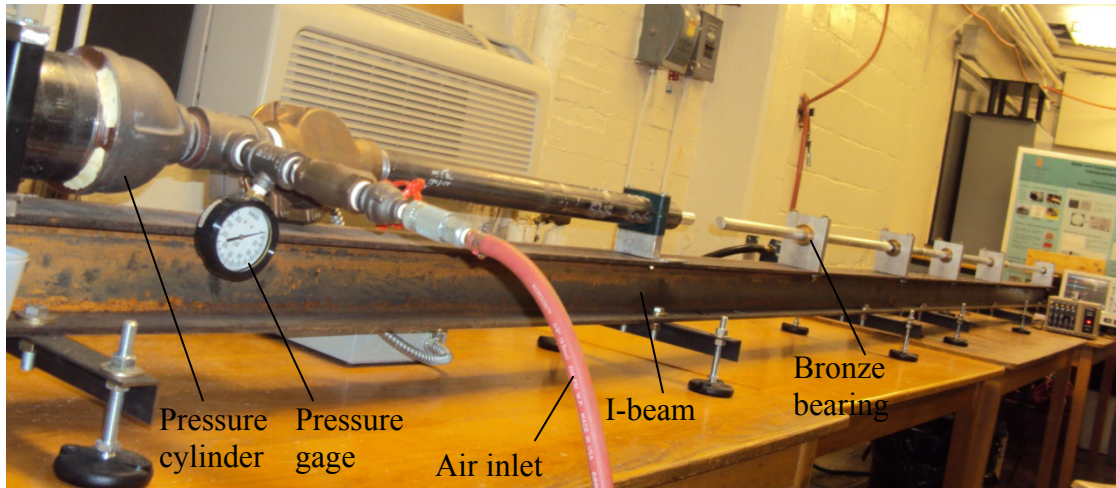
(b)
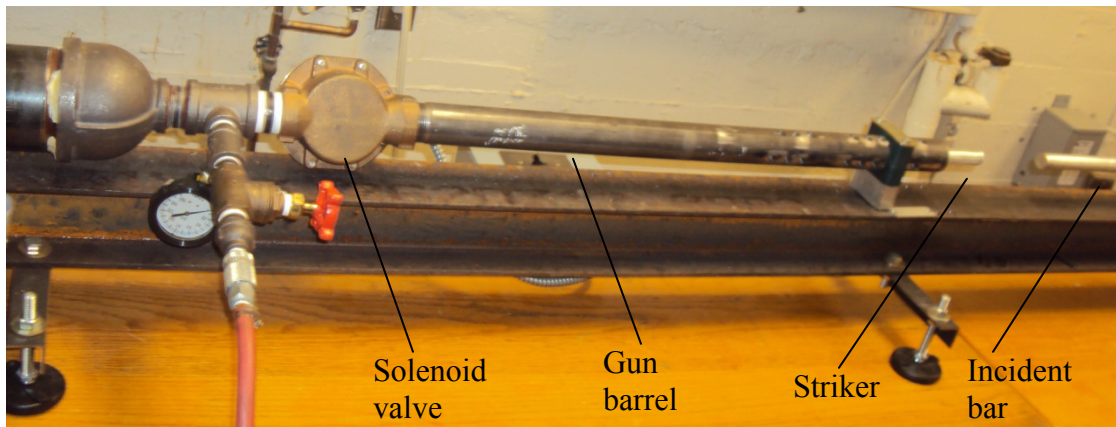
(c)
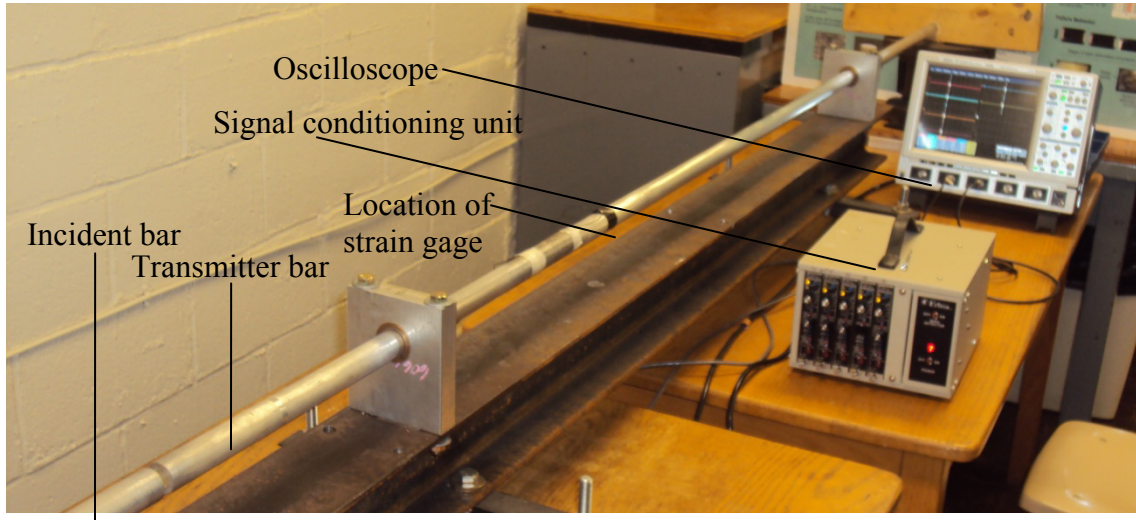
Figure 4.1: Photographs of the actual SHPB setup used for dynamic compression experiments

4.1 Experimental setup

Figures 4.1 and 4.2 show photographs and a schematic of the SHPB setup. It consists of an air pressure cylinder with a barrel, a striker (25.4 mm diameter and 406 mm long), a pulse shaper, an incident bar (25.4 mm diameter and 2438 mm long), a transmitter bar (25.4 mm diameter and 2438 mm long), a stopper, two strain gages (one on each bar), a signal conditioning unit (Ectron^{TM} Wheatstone bridge with signal conditioning amplifiers) and a data acquisition system (LeCroy^{TM} high-speed digital oscilloscope).

The cylinder, barrel and the bars were all mounted on two steel I-beams supported by adjustable legs. The adjustable legs were used for the leveling and aligning the bars. A solenoid valve was connected the cylinder and the barrel was used to launch the striker. The solenoid valve was encased within a μ-metal sheet to attenuate the magnetic flux field that would otherwise generate electrical noise in the output signals and trigger the

data acquisition circuit prematurely. A series of through holes were drilled into the end of the gun barrel so that when the striker was launched, the air ahead of the striker escaped through the holes laterally and the air resistance on the striker was minimized. To reduce friction, the incident and transmitter bars were supported on a series of bronze bearings mounted on the I-beams. Both the striker and the two bars were made of Al-7075 of the same diameter in order to eliminate the impedance mismatch between them. The 7075 aluminum alloy was chosen for its strain rate independent characteristics.

The sample was held snugly in between the incident and the transmitter bars prior to loading. The sample ends were coated with a thin layer of grease to position the sample and minimize friction at the interfaces. A 6.4 mm diameter disc made of a stack of four sheets of adhesively backed copper tapes each 0.1 mm thick was used at the front end of the incident bar as the pulse shaper. The interface between the pulse shaper and the incident bar was also coated with grease for tackiness. The use of pulse shaper helped to achieve dynamic stress equilibrium (to be described later) in the sample for the loading duration. The pulse shaper, the incident bar, the sample and the transmitter bar were all pushed against each other so that there were no gaps at any of the interfaces.
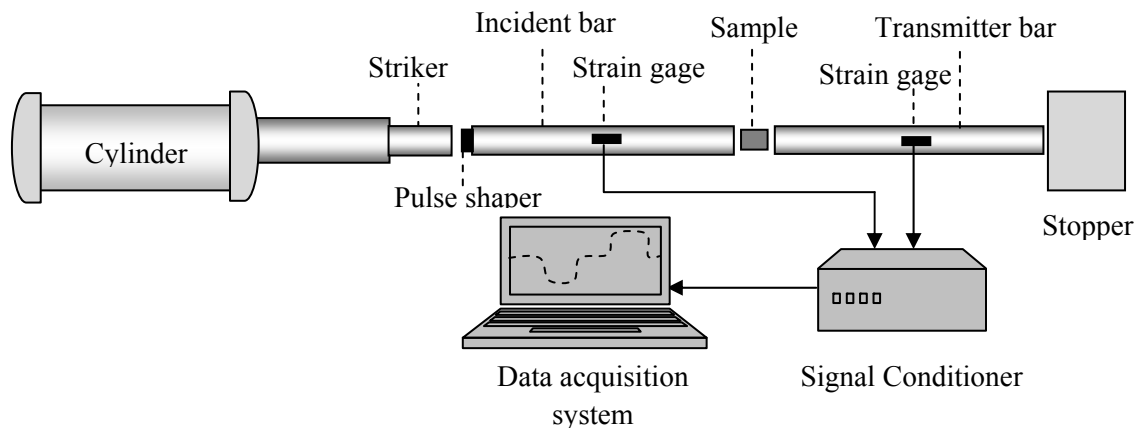
Figure 4.2: Split Hopkinson pressure bar setup

The strain histories in the bars were captured by two strain gages fixed one on each bar. The strain gages (CEA-13-062UW-350) had a grid resistance of 350Ω and a gage length of 1.6 mm (0.062 in) and were purchased from Vishay® Micro-Measurements®. One practical problem while conducting experiments was that the lead wires from the strain gages were breaking off at the terminals on the gages due to the intense stress waves. To overcome this, one long piece of masking tape was used to first wind the lead wires together. Then, the wire pair was attached to the bar using the remaining free end of the tape which was wrapped around the bar. In addition to the gages on the bars, two external dummy gages of the same specifications were mounted on an unstressed bar placed in the same atmospheric conditions as the incident and the transmitter bars. The leads from the strain gages on the bars and the external dummy gages were connected to the signal conditioning unit. The output from the signal conditioning unit was connected to the digital oscilloscope. The strain gage signals were filtered using a built in ("Eres" or Enhanced resolution filter) filter available in the oscilloscope. A resolution enhancement of 1.5 bits was chosen. The filtered data was then used to calculate the actual strain in both the bars as a function of time.

The striker was pushed all the way to the back of the gun barrel, and the pulse shaper was fixed on the incident bar. The sample was then held between the bars and they were all pushed against the stopper at the end of the transmitter bar. Next, the air cylinder was pressurized and the striker was launched towards the incident bar by opening the solenoid valve using an electrical switch. When the striker impacted the incident bar, a compressive stress wave (incident wave) originated at the front end of the bar and traveled towards the sample. A part of the stress wave (transmitted wave) traveled into

the sample and subsequently into the transmitter bar. Simultaneously, a portion of the stress wave was reflected (reflected wave) at the incident bar-sample interface and traveled back into the incident bar as a tensile stress wave. All three pulses were captured by the two strain gages mounted on the incident and the transmitter bars, and recorded as voltage histories in the data acquisition system after being processed by a signal conditioning unit[1]. The oscilloscope acquired the strain signals as voltage histories at a rate of 2.5×10^6 samples per second. These voltage histories were then used to calculate the strain histories of the bars.

4.2 Location of Strain Gages

The location of the strain gages on the incident bar was chosen based on the elastic wave speed (C_0) in the bar, the time period of the wave and the total length of the bar (L_{bar}) to make sure that there was no overlapping of the incident and the reflected stress wave signals. The bar wave speed $\left(\propto \sqrt{\dfrac{E}{\rho}} \right)$ in the Al 7075 bars is 5123 m/s [16], the striker length ($L_{striker}$) was 406.4 mm (16 in) and the length of the bars (L_{bar}) were 2438.4 mm (96 in). From the above data, the time period (T) [34] of the stress wave pulse was calculated as $\dfrac{2L_{striker}}{C_0} = 160$ μs. Then, the time taken by the wave to traverse the incident bar once was calculated as $\dfrac{L_{bar}}{C_0} = 475$ μs.

---

[1] To ensure that the circuitry and output voltage values from the signal conditioning unit were correct, a strain gage of the same specifications was mounted on a cantilever beam and the strains for various loads were measured. These measured strains were compared against theoretically calculated strains based on the one-dimensional beam equations, and the error factor was determined. This error factor was multiplied to the output voltages corresponding to the gages on the incident and the transmitter bars to ensure accuracy.
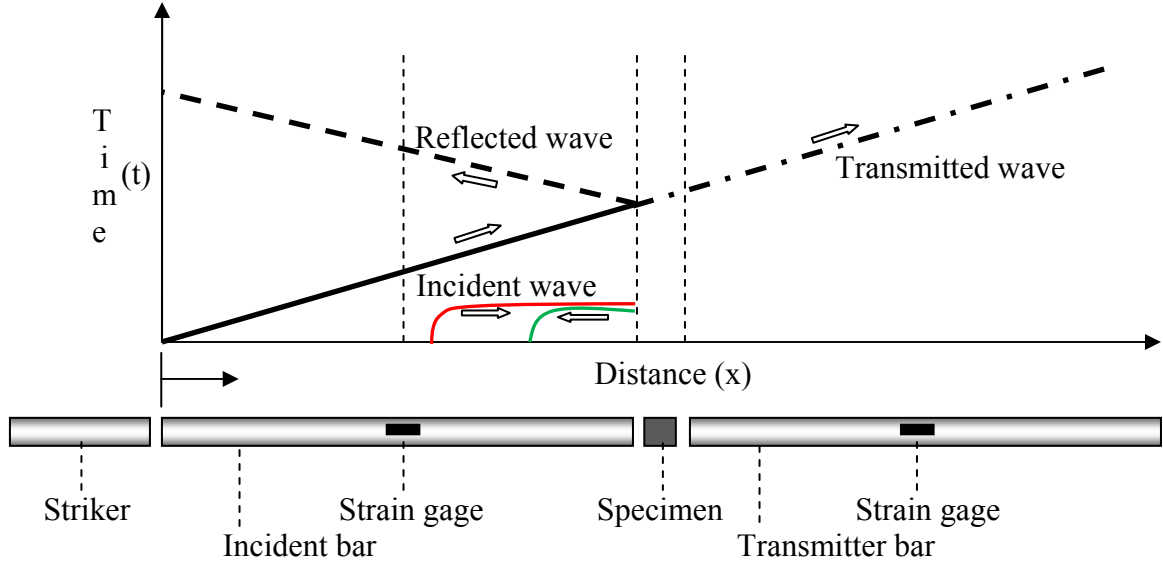
Figure 4.3: Schematic representation of the locations of incident, reflected and
transmitted waves in a SHPB setup

From the above calculations, it is evident that the time period of the wave
corresponds to twice the length of the striker. So, the strain gage on the incident bar was
located at approximately 1200 mm from the incident bar–specimen interface which is
more than twice the length of the striker. The schematic representation of the above
discussion is shown in Fig. 4.3 using the so-called *x-t* diagram. Accordingly, the incident
and the reflected wave signals will not overlap during a typical test.

4.3 Measurement of strain

The strain gages on the bars were separately connected to Wheatstone bridge
circuits in the signal conditioning unit. A half-bridge circuit was used in this study. The
external dummy gage of the half bridge circuit was mounted on a rod of the same
material as the bars so that the temperature effects on the working gage would be
nullified. The rod with the dummy gage was placed in the vicinity of the bars so as to

maintain the same atmospheric conditions. The strain in the bars is recorded as voltages, V_0 using the oscilloscope. If S_g is the gage factor of the strain gage, ε is the strain in the bar and R_g is the resistance of the strain gage, then change in resistance ΔR_g in the strain gage is given by,

$$\frac{\Delta R_g}{R_g} = S_g \varepsilon .$$ (4.1)

The output voltage for an initially balanced bridge V_0 when the gain or amplification is G, is given by

$$V_o = \frac{V_e G}{4} \frac{\Delta R_g}{R_g}$$ (4.2)

where V_e is the excitation voltage for the bridge. From the last two equations, the strain can be expressed as,

$$\varepsilon = \frac{4V_o}{V_e S_g G} .$$ (4.3)

4.4 Stress, strain and strain rate

The stress $\sigma(t)$, strain rate $\dot{\varepsilon}(t)$ and strain $\varepsilon(t)$ histories of the sample were calculated using the split Hopkinson bar equations. The details of the derivation [34] of the equations are provided as follows.
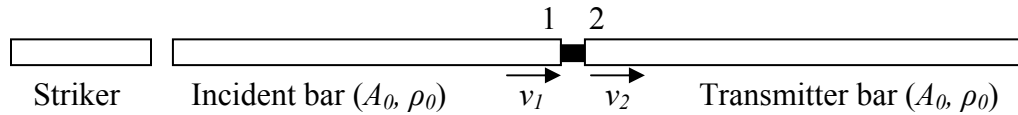
Figure 4.4: Schematic illustration of the SHPB

The strain rate or the rate of change of linear dimension in the specimen is given by

$$\dot{\varepsilon} = \frac{d\varepsilon}{dt} = \frac{v_1(t) - v_2(t)}{L} \ . \qquad (4.4)$$

As seen in Fig. 4.4, v_1 and v_2 are interface velocities at 1 and 2 and L is the specimen length. At the interfaces, at $t = 0$,

$$v_1 = C_0\varepsilon_I \ , \ v_2 = C_0\varepsilon_T \qquad (4.5)$$

where C_0 and C are the wave speeds in the bars and the specimen, respectively, and the subscripts I, R (and T) denote incident, reflected and transmitted, respectively. At $t > 0$, v_1 is reduced because of the reflected wave. That is,

$$v_1 = C_0(\varepsilon_I - \varepsilon_R) \ . \qquad (4.6)$$

From Eqs. (4.4), (4.5) and (4.6), the strain-rate expression can be re-written as,

$$\dot{\varepsilon}(t) = \frac{C_0(\varepsilon_I - \varepsilon_R) - C_0\varepsilon_T}{L} \ .$$

The strain in the specimen can be obtained by integrating the strain rate:

$$\varepsilon(t) = \frac{C_0}{L} \int_0^t \{\varepsilon_I(t) - \varepsilon_R(t) - \varepsilon_T(t)\} dt. \qquad (4.7)$$

By assuming stress equilibrium in the specimen at all times from 0 to t, the stress in the sample can be written as the average of the stresses on the specimen at the two interfaces as,

$$\sigma = \frac{P_1(t) + P_2(t)}{2A}$$

where,

$$P_1(t) = A_0 E_0 (\varepsilon_I + \varepsilon_R) \ ,$$

$$P_2(t) = A_0 E_0 \varepsilon_T \ .$$

Here, A_0 and A are cross sectional areas of the bars and specimen, respectively, and E_0 is the elastic modulus of the bars. Thus,

$$\sigma = \frac{A_0 E_0}{2A}\{\varepsilon_I(t) + \varepsilon_R(t) + \varepsilon_T(t)\}.$$

For dynamic equilibrium, $P_1(t) = P_2(t)$ and $\varepsilon_I + \varepsilon_R = \varepsilon_T$. Hence, we get,

$$\sigma(t) = E_0 \frac{A_0}{A} \varepsilon_T(t), \tag{4.8}$$

$$\dot{\varepsilon}(t) = -\frac{2C_0}{L}\varepsilon_R, \tag{4.9}$$

$$\varepsilon(t) = -\frac{2C_0}{L}\int_0^t \varepsilon_R \, dt. \tag{4.10}$$

The last three equations (4.8), (4.9) and (4.10) are the governing equations of the SHPB and were used to calculate the stress, strain and strain rate in the specimen as a function of time, and subsequently, to obtain stress-strain curves. Once the engineering stresses (σ_{eng}) and strains (ε_{eng}) were obtained, constant volume approximation was invoked to obtain the corresponding true stress (σ_{true}) and true strain (ε_{true}) values using:

$$\varepsilon_{true} = -ln\left(1 - \varepsilon_{eng}\right), \tag{4.11}$$

$$\sigma_{true} = \sigma_{eng}\left(1 - \varepsilon_{eng}\right). \tag{4.12}$$

5   EVALUATION OF THE SETUP

The SHPB setup developed in the laboratory was tested for its ability to produce a constant strain rate, dynamic stress equilibrium and experimental repeatability. Strikers of different lengths, ranging from 8 inches to 16 inches, were used to check the appropriate striker lengths for ensuring that the samples would undergo an appreciable strain/deformation within one stress pulse. In this chapter, the above issues are presented in addition to the calibration tests of the setup.

5.1 Dynamic equilibrium and constant strain rate

The standard SHPB equations for strain rate, strain and stress in the specimen assume that the specimen is under dynamic stress equilibrium and experiencing a constant strain rate during deformation. The dynamic stress equilibrium essentially means that the instantaneous forces at the front and back ends of the specimen are equal. That is, the sum of the strains or output voltages corresponding to the incident and reflected stress waves should equal the strain or output voltage corresponding to the transmitted wave. In real situations, however, this does not occur unless the rate of loading is reduced to allow sufficient time for the specimen to reach dynamic equilibrium. This is often achieved by the use of so-called pulse shapers. A pulse shaper essentially moderates the initial impact allowing sufficient time for the specimen to attain stress equilibrium before undergoing

large deformation. So, different types of pulse shapers were used in this work at the striker / incident bar interface to attain the best possible dynamic equilibrium in the sample.
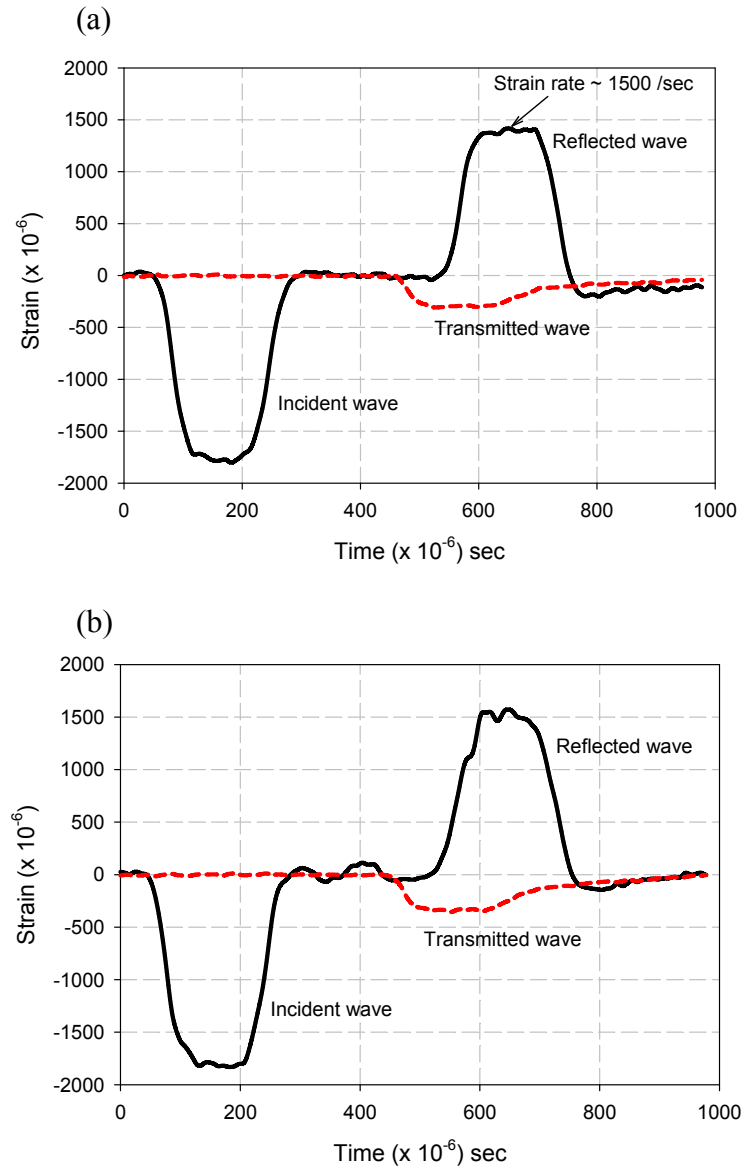
Figure 5.1: Representative SHPB strain histories for (a) Syntactic foam sample with 30% microballoon volume fraction, (b) IPC foam sample with 30% microballoon volume fraction

The pulse shapers made of a stack of copper tapes that are more compliant than aluminum resulted in reducing the rate of loading and smoothing the instantaneous input strain wave profile as seen in Fig. 5.1. The representative strain histories for SF-30 and IPC-30 samples obtained by using the above mentioned pulse shaper that resulted in good dynamic stress equilibrium are shown in Fig. 5.1. In Figs. 5.1(a) and (b), the solid line corresponds to the strain history in the incident bar, and the dotted line corresponds to the one in the transmitter bar. As can be seen from the strain histories, the initial compressive wave ramps up for about 20 microseconds to attain the maximum amplitude instead of an instantaneous jump. Subsequently, the amplitude remains constant for about 125 μs before starting to ramp down. The tensile reflected wave from the incident bar / specimen interface reaches the strain gage on the incident bar at approximately 250 μs after the end of the incident wave. The transmitted wave is seen as a compressive signal in Fig. 5.1, and it lasts for almost 125 μs before its amplitude starts to ramp down.

The condition that the sample should be under a constant strain-rate during the deformation was verified by plotting the sample strain-rate histories (Figs. 5.2(a) and (b)). The equations [34] for SHPB reveal that the strain rate in the specimen is proportional to the reflected wave induced strain in the incident bar. The nearly constant strain region in the reflected wave (Fig. 5.1) suggests that the specimen was under a constant strain rate for about 125 μs during the dynamic loading event. The strain-rate histories shown in Figs. 5.2 (a) and (b) for the representative SF-30 and IPC-10 samples confirm this. As was the case for the incident (as well as reflected) strain waves, the strain-rate histories also follow the ramp-up and ramp-down patterns during the initial

and final stages of the pulses, respectively. Also, it is evident that the strain-rates remain

nearly constant for about 125 μs for both SF and IPC cases.
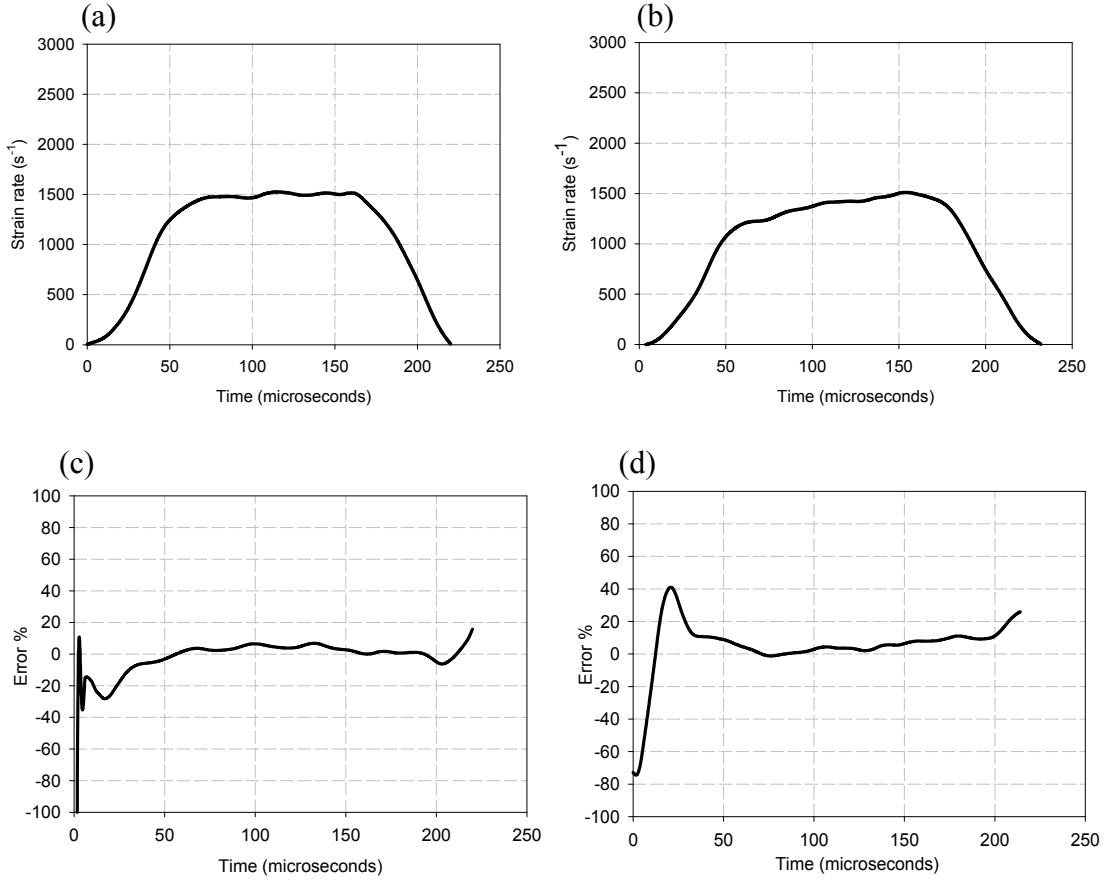
Figure 5.2: Demonstration of constant strain-rate for (a) SF-30 and (b) IPC-10,

and dynamic stress equilibrium for (c) SF-30 and (d) IPC-10

The dynamic stress equilibrium condition was verified by plotting the percentage

difference between the incident wave and the (reflected + transmitted) wave with respect

to the incident wave. From Figs. 5.2(c) and (d), it can be seen that the percentage

difference is about 9% or less for most part of the loading pulse duration and that the

dynamic equilibrium condition is satisfied quite well given the highly transient nature of

30

the dynamic event. Among the various shapers that were tried (Fig. 5.3), a stack of four 0.25 inch diameter copper tapes resulted in good equilibrium and was used in all experiments unless stated otherwise.

5.2 Effect of pulse shapers and striker length

As noted earlier, different types of pulse shapers were used at the striker / incident bar interface to attain the best possible dynamic equilibrium in the sample. The stress-strain curves corresponding to the different pulse shapers are shown in Fig. 5.3. From the figure, it can be seen that there is no significant difference in the stress-strain curve, even when different pulse shapers were used. The plots also confirm the repeatability of the experimental setup. Nevertheless, the pulse shaper that gave the best dynamic equilibrium of the test sample was used for all other experiments.
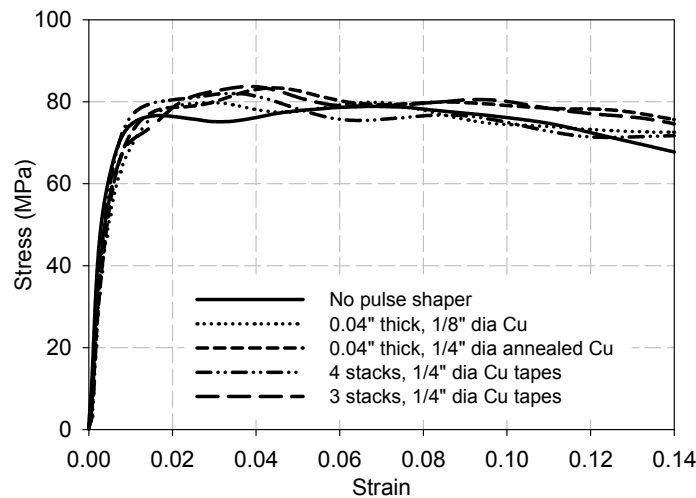
Figure 5.3: Effect of pulse shapers and repeatability on SF-30 samples
(strain-rate ~ 1500/s)

As mentioned at the beginning of this chapter, strikers of different lengths were used to test samples to select the most appropriate and practical striker length. From the discussion in Section 4.2 it is clear that the loading pulse duration is directly proportional to the striker's length when the striker and the bars are made of the same material. It should also be noted that the longer the loading pulse, the larger the sample deformation within the first pulse. This is evident from Fig. 5.4. The line-dot-dot patterned line corresponds to an 8 in. long striker. The maximum strain attained by the sample by using this striker was ~12%. Longer strikers of lengths 12 in. and 16 in. yielded higher strains of ~16% and ~20%, respectively. In Fig. 5.4, the line-line patterned line corresponds to the 12 in. striker and the line-dot-line patterned line corresponds to the 16 in. striker.
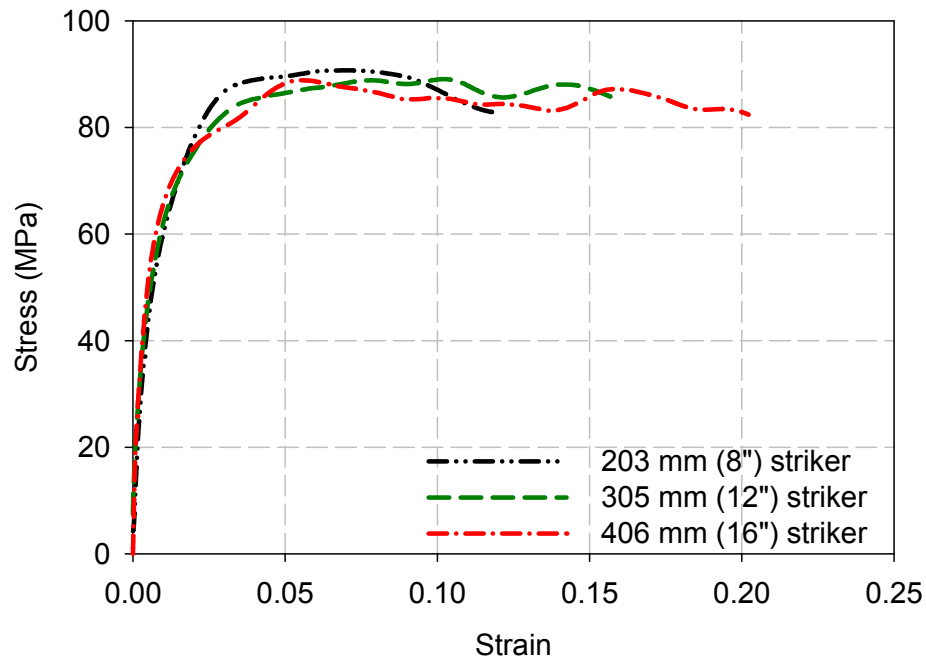
Figure 5.4: Effect of striker length on SF-30 samples (strain-rate ~ 1500/s)

5.3 SHPB calibration

Since the primary motivation for this study is to study low impedance materials, the SHPB apparatus was also calibrated relative to the published results [35] in the literature for a widely studied low impedance material. The material tested was a commercially produced cast acrylic rod stock of 12.7 mm dia. Cylindrical samples of length 6.35 mm were machined from the stock and tested under conditions similar to those used for SF and IPC samples. The resulting true stress-strain diagram for a strain rate of approximately 1250 /sec is shown in Fig. 5.5. The results are compared with those reported in Ref. [35] for specimens made from cast acrylic sheet stock of identical specimen dimensions.
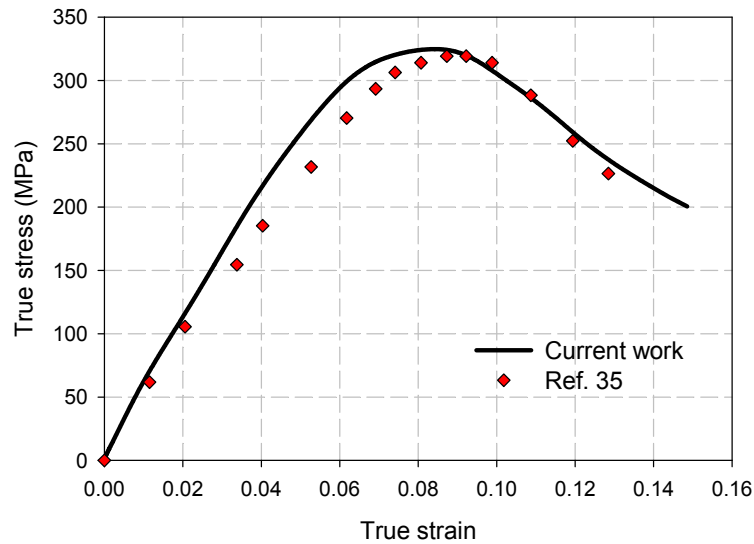
Figure 5.5: True stress-strain response for cast acrylic at a strain rate of ~ 1250 / sec

The overall similarity in the stress-strain response with the reported ones is clearly evident. The minor deviations are attributed to differences in the specimen preparation, stock material (sheet vs. rod) and strain rates (~ 1500 / sec in Ref. [35]).

6   EXPERIMENTAL RESULTS

This chapter presents the dynamic compression responses of SF and IPC obtained from the experiments. To appreciate the strain rate effects on these two material systems, quasi-static [2, 28] stress-strain responses of SF and IPC previously reported by Jhaver and Tippur [28] are presented first. Later, the dynamic stress-strain responses obtained from the current work are presented along with a comparative analysis of quasi-static and dynamic responses. Finally, a summary of the energy absorption characteristics of SF and IPC under quasi-static conditions [2, 28], which are also later compared against the corresponding results under dynamic conditions, is also presented.

6.1 Quasi-static compressive stress-strain response

6.1.1 Syntactic foam

The static compressive true stress vs. true strain responses for four types of syntactic foams (SF) (10, 20, 30 and 40% V_f) are shown in Fig. 6.1. These responses show three distinct stages of deformation typical of structural foams. An initial linear elastic region is followed by a distinct drop in stress with increasing strain after yielding. (This softening response is attributed to the one seen for neat epoxy sample tested under identical static loading conditions, and is presented in Appendix A.) With increasing strain, the softening response is followed by a region of nearly constant stress. In this

plateau region, microballoons within the SF fail progressively. Further increase in load causes densification (signified by an increasing stress) as microballoons collapse completely. As seen in Fig. 6.1, the stress-strain responses of syntactic foam samples of all four volume fractions follow a similar trend. It is also evident that the compressive strength decreases with increasing volume fraction of microballoons in the SF. The 10% V_f samples (SF-10) have a compressive strength of 63.2 MPa, whereas the SF-40 samples have 34.4 MPa, or a 45% decrease. (The elastic modulus values also show a decreasing trend with increasing microballoon volume fraction. The SF-10 samples have an elastic modulus of ~1600 MPa and the SF-40 samples, ~1260 MPa, which is a 21% decrease.) The true strains corresponding to the initial maximum stress are 4.5%, 4.0%, 3.3% and 3.1% for the SF-10, SF-20, SF-30 and SF-40 samples, respectively.
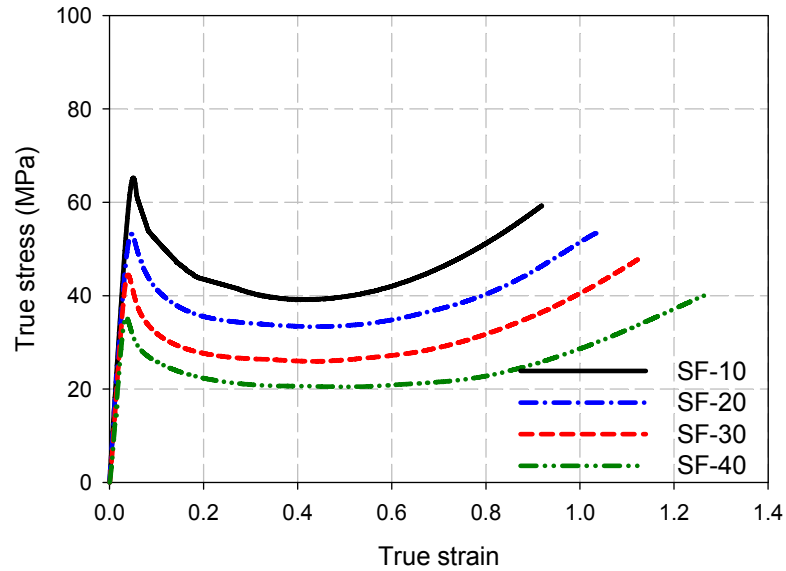
Figure 6.1: Effect of microballoon volume fraction on quasi-static

compression response of syntactic foam (SF) samples [2]

The plateau stress values of SF samples in the order of increasing volume

fractions are approximately 40 MPa, 33.5 MPa, 26 MPa and 20.6 MPa. This trend of

decreasing plateau stress with increasing microballoon volume fraction is also consistent

with those predicted by Kim and Plubrai [36]. Furthermore, as the volume fraction of

microballoons increase in SF, the densification strain also increases monotonically, from

~50% true strain for 10% V_f to ~75% true strain for 40% V_f. The deformed samples were

sectioned and examined in a scanning electron microscope. Figure 6.2 shows

micrographs of deformed SF-30 samples corresponding to 14% (Fig. 6.2(a)) and 58%

(Fig. 6.2(b)) strains.
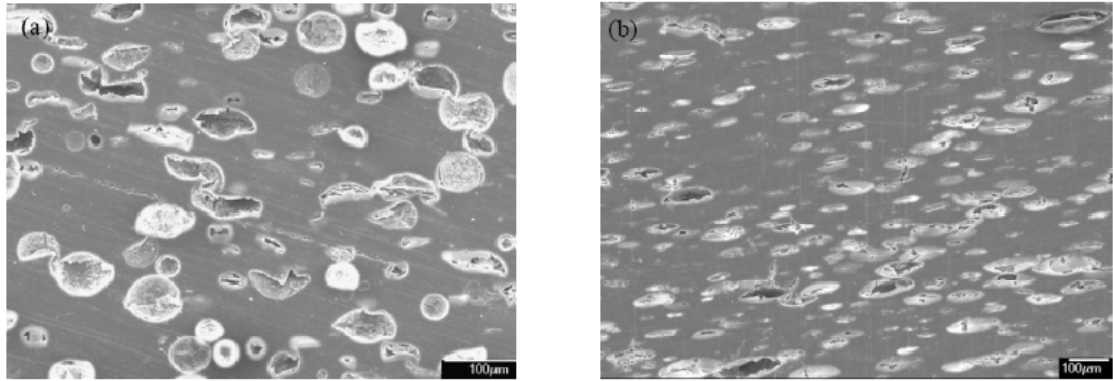
Figure 6.2: SEM images of 30% V_f syntactic foam at (a) 14% strain and (b) 58%

strain showing the crushing of microballoons at various stages of static

deformation. (The loading was in the vertical direction) [2]

The onset of microballoon failure is evident in Fig. 6.2(a). Figure 6.2(b) shows

the microballoons to be almost completely crushed and flattened, which explains the

densification or the increase in stress with increase in strain after ~50% strain.

Furthermore, compression of the matrix and crushing of microballoons is uniform in the

entire field of view. The direction of load in the micrographs is along the vertical axis, but a skew in the direction of the fractured microballoons is seen in Fig. 6.2(a) suggesting a tendency for shear failure.

6.1.2 IPC

The quasi-static results for four different IPC samples with different volume fraction of microballoons in SF (10%, 20%, 30% and 40%) are shown in Fig. 6.3. The IPC foams respond in a way similar to SF samples (Fig. 6.1). There is an initial linear elastic region, followed by yielding and softening signifying the onset of nonlinearity. The softening is then followed by regions of plateau stress and densification.
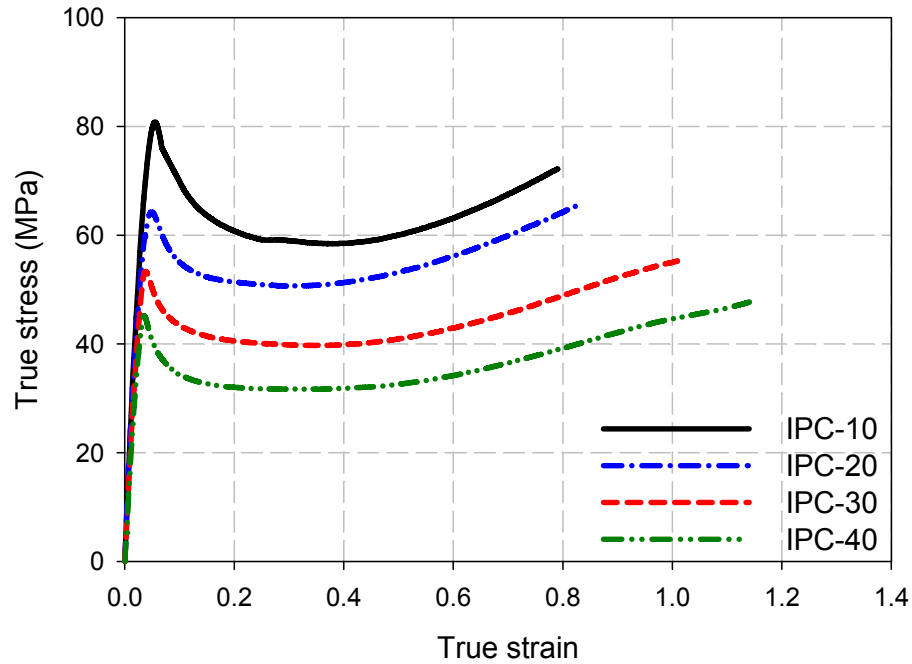
Figure 6.3: Effect of microballoon volume fraction on quasi-static compression

response of IPC foam samples [2]

In the case of IPC, however, the onset of nonlinearity is also affected by progressive bending of the aluminum ligaments, which in turn causes crushing of microballoons in between the ligaments (Fig. 6.4). The plateau region for IPC foam is relatively narrow when compared to the one for the corresponding syntactic foam. That is, densification starts at a relatively lower strain in IPC. The elastic modulus for 10%, 20%, 30% and 40% volume fraction IPC foam samples are 2354 MPa, 2123 MPa, 1852 MPa and 1702 MPa, respectively. The compressive strengths of the IPC samples in increasing order of volume fraction are 81.0 MPa, 63.1 MPa, 51.5 MPa and 44.0 MPa. The plateau stresses for the samples show a similar trend as the compressive strengths. That is, samples with a lower V_f of microballoons have higher plateau stresses. The true plateau stress values for the 10%, 20%, 30% and 40% V_f samples are approximately 59 MPa, 50 MPa, 40 MPa and 31 MPa, respectively, which is a ~10 MPa increase in plateau stress value for a 10% decrease in V_f of microballoons.
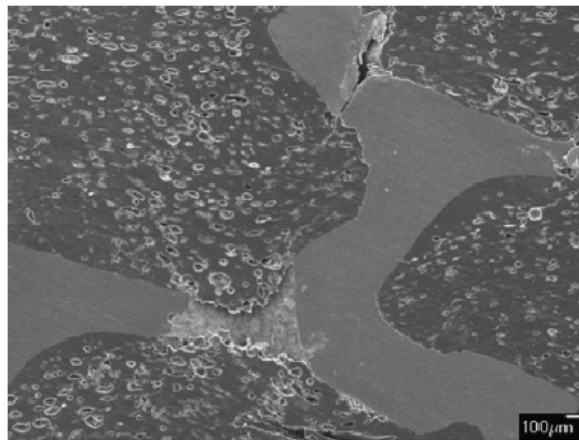
Figure 6.4: SEM image of statically deformed IPC foam at 58% strain.

(The loading was along the vertical direction) [2]

38

After yielding, the onset of densification also follows a uniform trend, wherein lower V_f samples have lower densification strain. The approximate true strain values which mark the onset of densification are in the 45%-55% range. The quasi-static compression properties are consolidated in Table 6.1.

Designation	Microballoon volume fraction (%)	Density (kg/m^3)	Compressive strength (MPa)	Elastic modulus (MPa)
SF-10	10	995	63 ± 1.6	1600 ± 25
SF-20	20	870	52 ± 2.2	1530 ± 35
SF-30	30	796	42 ± 1.4	1448 ± 28
SF-40	40	696	34 ± 1.8	1261 ± 42
IPC-10	10	1169	81 ± 1.6	2354 ± 26
IPC-20	20	1044	63 ± 2.3	2123 ± 32
IPC-30	30	986	52 ± 3.6	1852 ± 27
IPC-40	40	862	44 ± 1.9	1702 ± 26

Table 6.1: Quasi-static properties of syntactic foam and IPC foam samples

6.2 Dynamic compressive stress-strain response

SF and IPC samples with 10%, 20%, 30% and 40% microballoon volume fractions were tested at a strain rate of ~1500 per second using the split Hopkinson pressure bar described in the previous chapter. The maximum strain attained by a sample depends on the time period of the incident stress wave. This in turn depends on the length

of the striker used [34]. Several striker lengths, 203 mm (8 in.) – 406 mm (16 in.), were considered. In view of a relatively large expected strain to failure, the longest feasible striker length was considered. The incident stress pulse generated by the 406 mm long striker (impact velocity ~15 m/s) had a total time period of ~200 µs with a constant strain lasting over 100 µs as shown in the representative strain histories in Fig. 5.1 for SF and IPC samples with 30% volume fraction of microballoons. The maximum engineering strain experienced by the sample for this pulse was a little over 25%. So, conservatively, all analyses were based on a maximum specimen strain value of 25% and the stress-strain data once the stress pulse started dropping off was not considered in the analyses.

6.2.1 Syntactic foam

The dynamic true stress - true strain responses of SF with four different volume fractions of microballoons obtained using a 406 mm striker at a strain rate of ~1500 per second are shown in Fig. 6.5. The response of syntactic foam has two distinct regions. An initial linear elastic response is followed by a monotonically decreasing stress region with increasing strain. As in the quasi-static cases, the compressive strengths of the samples decrease with increasing microballoon volume fraction. The compressive strengths of the 10%, 20%, 30% and 40% volume fraction samples were approximately 104 MPa, 80 MPa, 62 MPa and 50 MPa, respectively. The relative decrease in the compressive strengths for every 10% increase in the microballoon volume fraction is ~20%. Among the notable differences, dynamic loading clearly suppresses the distinct softening seen in quasi-static cases after the initial peak stress in all volume fractions, as reported in Ref. [28]. Instead, a more gradual softening is evident in Fig. 6.5. The tendency for the SF

with lower volume fraction of microballoons (10% and 20%) to soften after attaining the maximum stress is somewhat more distinct than for those with higher volume fractions of microballoons (30% and 40%). These can be further attributed to the differences in neat epoxy response under static and dynamic loading conditions as described in Appendix A. After yielding, the stresses for SF with lower V_f of microballoons remain consistently higher than that for SF with higher V_f. The difference in stress values after yielding between specimens with different volume fractions of microballoons is approximately constant at all strains (within the observation window). The elastic responses under static and dynamic conditions also show differences. The measured elastic modulus for the four cases of syntactic foams is shown in Table 6.2.
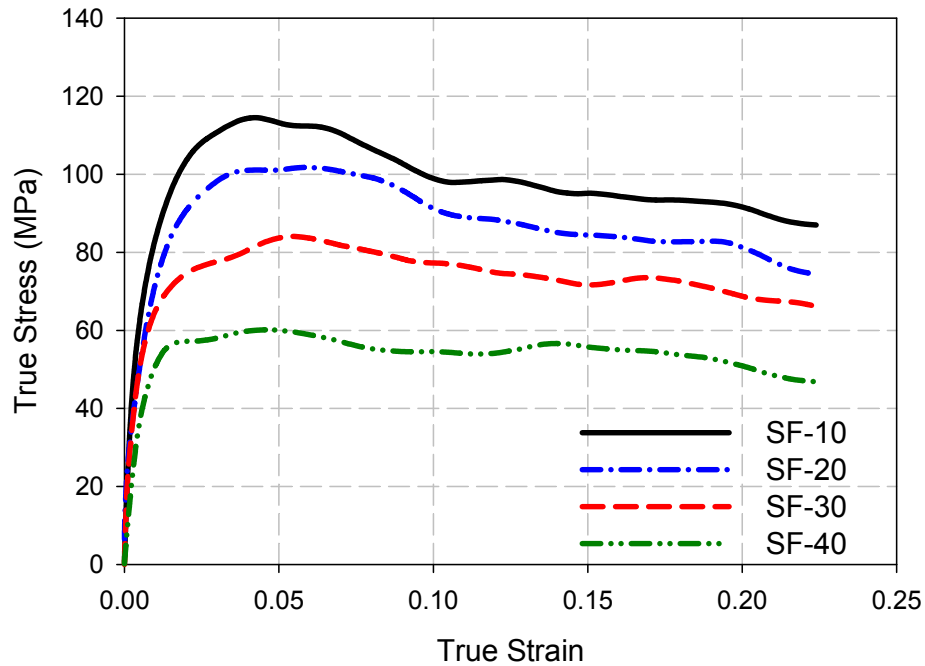
Figure 6.5: Effect of microballoon volume fraction on dynamic stress-strain response of SF samples (Strain rate ~1500/sec)

Designation	Microballoon volume fraction (%)	Density (kg/m^3)	Compressive strength (MPa)	Elastic modulus (MPa)
SF-10	10	995	104 ± 4	3460
SF-20	20	870	80 ± 3	3100
SF-30	30	796	62 ± 5	2700
SF-40	40	696	50 ± 3	2400
IPC-10	10	1169	120 ± 4	-
IPC-20	20	1044	100 ± 5	-
IPC-30	30	986	80 ± 6	-
IPC-40	40	862	60 ± 3	-

Table 6.2: Dynamic properties of syntactic foam and IPC foam samples

It should be noted that the dynamic elastic modulus values shown in Table 6.2 were obtained using ultrasonic pulse-echo measurements [37]. (This method was preferred over direct measurement from the stress-strain response due to weak stress equilibrium in the specimen during the initial stages (up to about 30 μs) of stress wave propagation in the specimen. The elastic moduli of the IPC are not reported here as the pulse-echo transducer could not be used effectively to determine wave speeds in IPC due to wave dispersion problems). The results indicate a higher elastic modulus under dynamic conditions when compared to the respective quasi-static [28] counterparts. A backlit photograph of a deformed SF sample with 30% V_f of microballoons is shown in

Fig. 6.6(a). The sample in this case was loaded along the vertical direction. A network of shear bands crisscrosses the entire sample and the bands are oriented at approximately ±45° to the loading direction.

Figure 6.6: (a) Side view of a dynamically deformed syntactic foam sample revealing a network of shear bands, (b) SEM image of cross section of dynamically deformed syntactic foam; Careful observation reveals crisscrossing shear failure planes. (The loading was along the vertical direction)

A micrograph of a 30% V_f specimen is shown in Fig. 6.6(b). Again, the direction of loading was along the vertical direction of the image. The cracks that appear in the image are skewed at an angle of approximately 45° to the direction of application of the load suggesting failure due to shear localization. In regions away from the crack, the microballoon footprints are essentially circular suggesting very little deformation away from the shear bands.

6.2.2 IPC

The IPC samples of four microballoon volume fractions *viz.* 10% (IPC-10), 20% (IPC-20), 30% (IPC-30) and 40% (IPC-40) were tested and the results are shown in Fig.

6.7. The dynamic compression response of IPC foams followed trends similar to that of the corresponding syntactic foams. The response shows a linear region in the beginning, followed by a modest nonlinear response until a maximum stress is reached. Subsequently a monotonic reduction of stress with increasing strain is seen in the observation window up to 22% true strain. As in the case of SF samples, the yield strengths of IPC samples decrease with increasing volume fraction of microballoons.
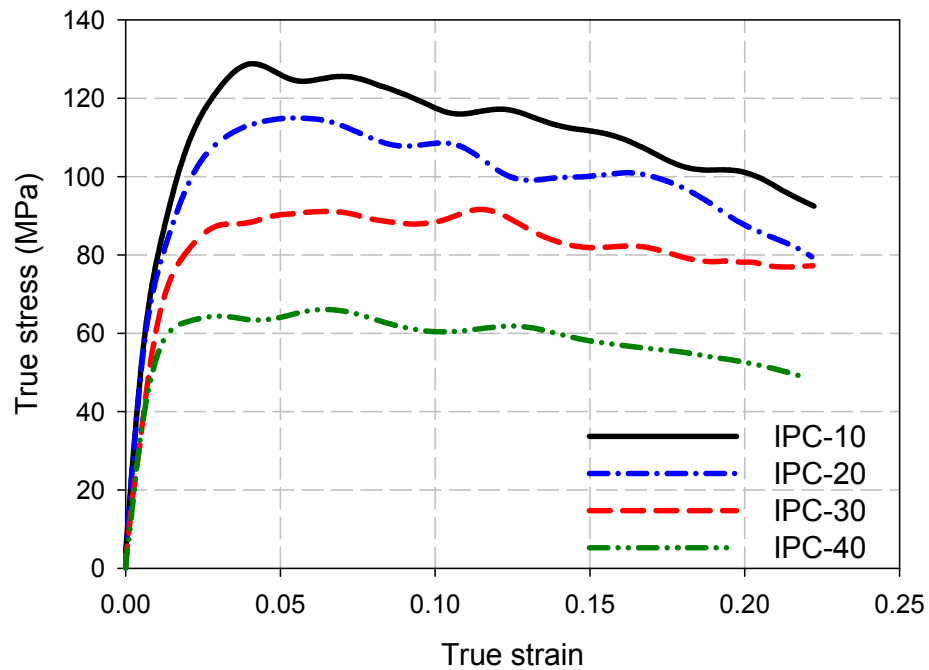
Figure 6.7: Effect of microballoon volume fraction on dynamic stress-strain response of IPC foam samples (Strain rate ~1500/sec)

In the order of increasing microballoon V_f, the maximum stress values attained are approximately 120 MPa, 100 MPa, 80 MPa and 60 MPa. The percentage decrease in the compressive strength for the IPC-20 with respect to that of IPC-10 is 17%, and that of IPC-30 with respect to that of IPC-20 is 20%. The IPC-40 has a 25% decrease in

compressive strength with respect to the IPC-30. Figure 6.8 shows a photograph and a micrograph of a deformed 40% V_f IPC. As in the SF samples, the photograph of the deformed sample in Fig. 6.8(a) clearly shows a well-defined network of shear bands throughout the specimen (the shear bands are slightly more pronounced and father apart relative to the SF counterparts due to the presence of the aluminum network.). The SEM image in Fig. 6.8(b) shows underlying microscopic failure mechanisms in the IPC. Two types of failures can be identified from this image. One is the formation of cracks in the syntactic foam (similar to the one seen for SF in Fig. 6.6(b)). The crack in Fig. 6.8(b) is again inclined at ±45° to the direction of the load along the vertical direction of the image, which suggests that the failure occurred due to shear localization. However, shear bands here are interrupted by the metallic ligaments of the IPC. The other type of failure in IPC, which is absent in pure SF samples, is the debonding of the interfaces between the syntactic foam and the aluminum ligaments.

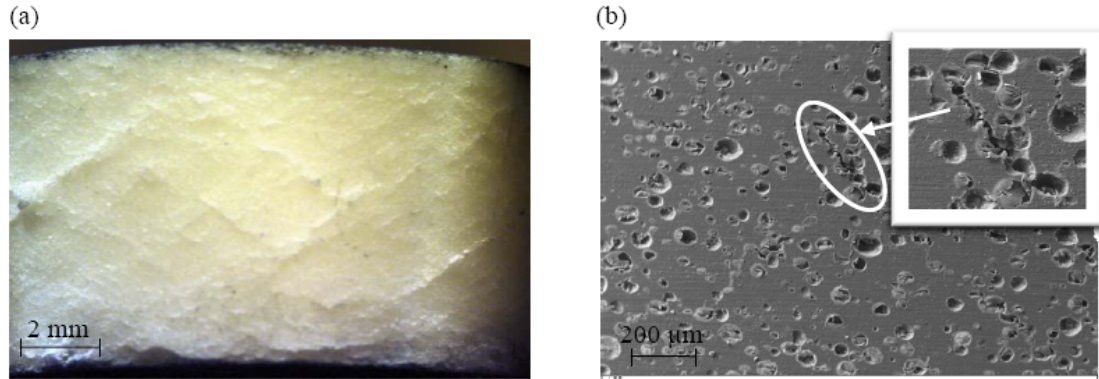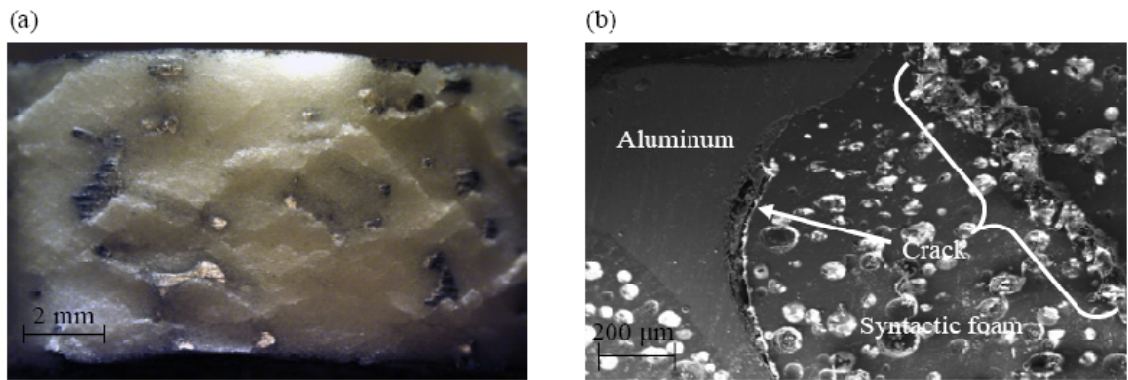Figure 6.8: (a) Side view of a dynamically deformed IPC foam sample revealing multiple shear bands and (b) SEM image of the cross section of dynamically deformed IPC foam. (The loading was along the vertical direction)

6.3 Energy absorption

An aspect of foams that is attractive for structural applications is energy absorption. A comparison of energy absorbed per unit volume and per unit mass by the SF and the corresponding IPC samples under dynamic loading conditions was made. The energy absorbed per unit volume (U) was evaluated by calculating the area under the true stress – true strain curve as,

$$U = \int_0^\varepsilon \sigma(\varepsilon)d\varepsilon \tag{6.1}$$

where $\sigma(\varepsilon)$ is the stress as a function of strain. The energy absorbed was evaluated up to a strain value of 22% as $U_{0.22}$. The energy absorption per unit mass was also evaluated by dividing the energy absorbed per unit volume by the density of the sample. Again, to appreciate the effect of strain rate on energy absorption, the quasi-static results on energy absorption [2, 28], are presented before the dynamic counterparts.

6.3.1 Quasi-static

The absorbed energy ($U_{0.22}$) evaluated from true stress-true strain graphs [2, 28] is plotted as histograms for all the cases in Fig. 6.9. As was the case for the compressive strength and the elastic modulus, the absorbed energies also show a decreasing trend with increasing volume fraction of microballoons. The energy absorbed per unit volume (Fig. 6.9 (a)) by the SF samples of 10%, 20%, 30% and 40% microballoon V_f are 10.4 MJ/m^3, 8.5 MJ/m^3, 6.8 MJ/m^3 and 5.4 MJ/m^3, respectively. The relative decrease in $U_{0.22}$ for every 10% increase in microballoon V_f is 18-20%. The energy absorbed by the IPC samples is higher than that by the corresponding syntactic foam samples by 34%-37%. The actual values are approximately 14.0 MJ/m^3, 11.5 MJ/m^3, 9.2 MJ/m^3 and 7.4 MJ/m^3

for 10%, 20%, 30% and 40% cases, respectively. The percentage decreases in $U_{0.22}$ for the IPC-20 / IPC-10 pair, IPC-30 / IPC-20 pair and the IPC-40 / IPC-30 pair are approximately 20% in each case.

(a)

(b)

Figure 6.9: Energy absorbed (a) per unit volume and (b) per unit mass by SF and IPC foam samples under quasi-static loading up to 22% true strain

The energy absorption per unit mass are plotted in Fig. 6.9(b) and they also show a similar trend. The IPC samples have absorbed 12.0 kJ/kg, 11.0 kJ/kg, 9.4 kJ/kg and 8.6 kJ/kg which are higher when compared to the syntactic foams of corresponding volume fraction of microballoons, respectively. The percentage increase in the energy absorption per unit mass in the IPC foams with respect to the syntactic foams is approximately 10%-14%.

6.3.2 Dynamic

The data on energy absorption, $U_{0.22}$, under dynamic loading conditions is shown in Fig. 6.10. The absorbed energies of SF and IPC foam samples under dynamic loading conditions are clearly higher than those observed under quasi-static loading conditions (Fig. 6.9). Energy absorbed per unit volume by SF-10, SF-20, SF-30 and SF-40 samples are 21.9 MJ/ m^3, 19.6 MJ/m^3, 16.4 MJ/m^3 and 12.1 MJ/m^3, respectively and that by IPC-10, IPC-20, IPC-30 and IPC-40 samples are 24.5 MJ/m^3, 22.0 MJ/m^3, 18.3 MJ/m^3 and 12.7 MJ/m^3, respectively. The percentage reduction in $U_{0.22}$ per unit volume for the SF-20 / SF-10 pair, SF-30 / SF-20 pair and the SF-40 / SF-30 pair are approximately 11%, 16% and 26% respectively. The percentage reduction in $U_{0.22}$ per unit volume for the IPC-20 / IPC-10, IPC-30 / IPC-20 pair and the IPC-40 / IPC-30 pair are approximately 10%, 17% and 30%, respectively. The trend of the percentage reduction in the energy absorption per unit volume suggests that the rate of reduction in $U_{0.22}$ would be greater than the rate of increase in the microballoon volume fraction for dynamic loading.
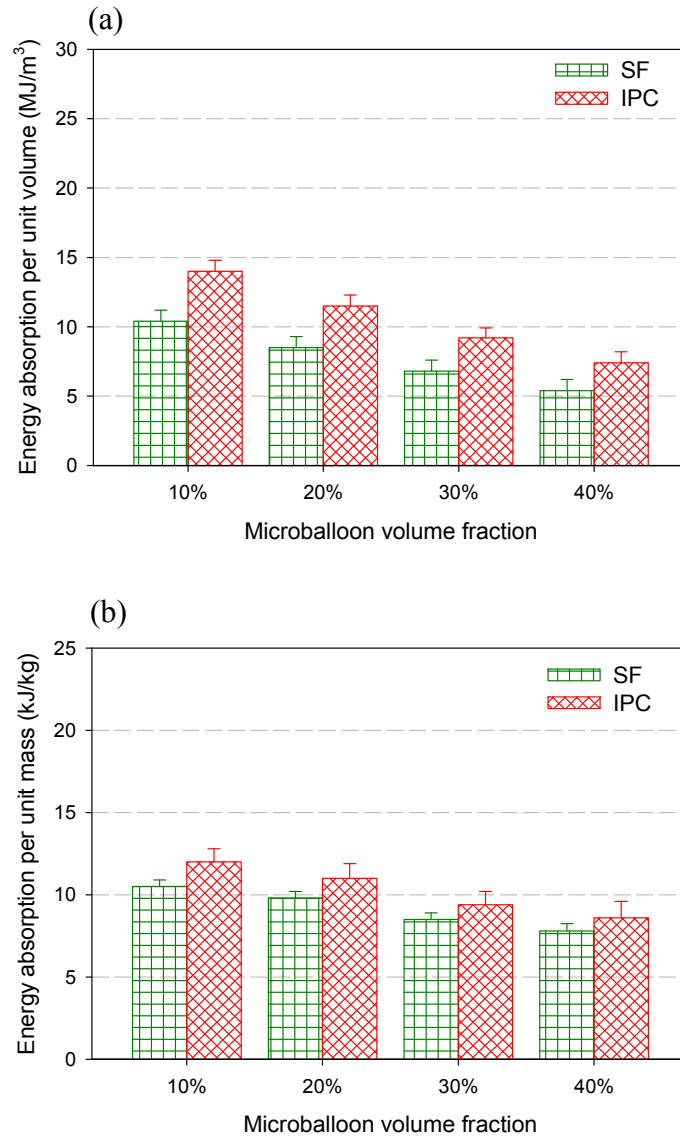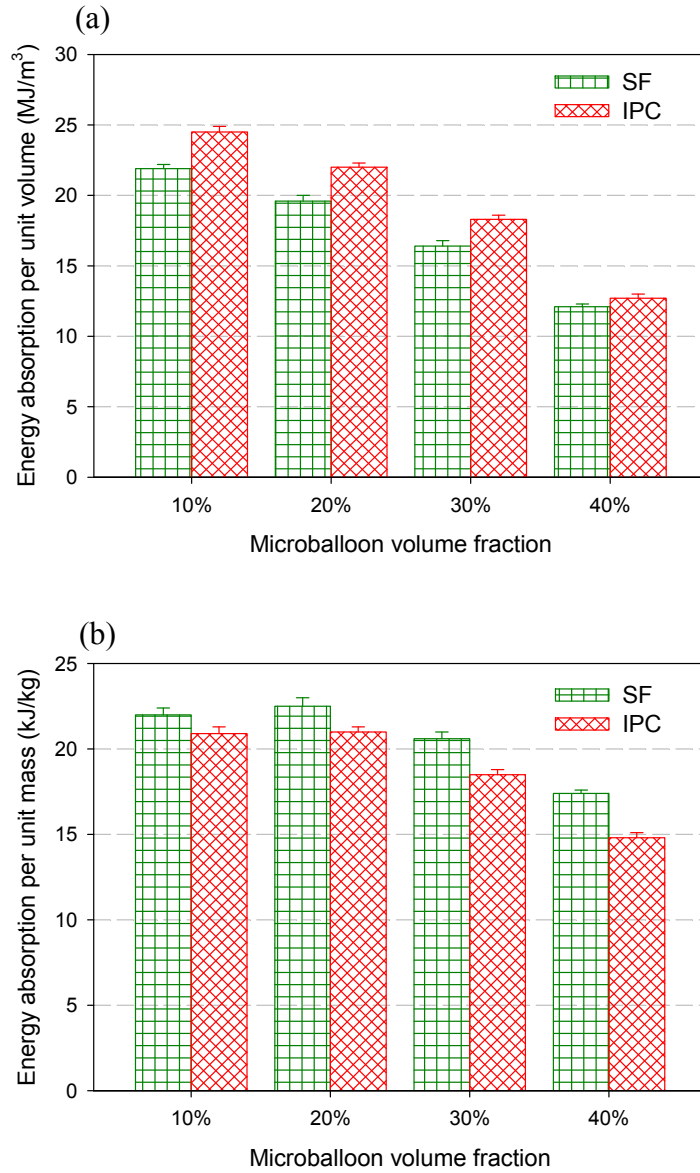
Figure 6.10: Energy absorbed (a) per unit volume and (b) per unit mass by SF and

IPC foam under dynamic loading up to 22% true strain

However, in the case of energy absorbed per unit mass, the syntactic foam

appears to perform better than the corresponding IPC foam under dynamic loading

conditions. The energies absorbed per unit mass by the SF-10, SF-20, SF-30 and SF-

40 samples were 22.0 kJ/kg, 22.5 kJ/kg, 20.6 kJ/kg and 17.4 kJ/kg, respectively and that absorbed by IPC-10, IPC-20, IPC-30 and IPC-40 samples were 20.9 kJ/kg, 21.0 kJ/kg, 18.5 kJ/kg and 14.8 kJ/kg, respectively. Again, these are nearly twice the respective quasi-static values. When compared with the SF samples, the IPC samples had lower energy absorption per unit mass by 5%, 6.7%, 10.2% and 14.5%, respectively. (It should be noted that the differences between 10% and 20% SF and between the SF and IPC of the two volume fractions are relatively small with overlapping error bars. Hence, no claim regarding the trend between these two volume fractions is made.)

Accordingly, *if energy absorption at a slight increase (~10%) in weight is acceptable for an application, IPC still outperforms SF even under dynamic conditions*. Another interesting observation is that the increasing trend of the energy absorption per unit mass with decreasing microballoon volume fraction appears to be reversed at a microballoon volume fraction of approximately 10%. Therefore, the 10% microballoon volume fraction could be the threshold level in terms of absorbed energy per unit mass.

6.3.3   Dynamic energy absorption history

Plots of cumulative absorbed energy at various strain values were also plotted to evaluate the history of energy absorption during dynamic compression. The variations in energy absorption per unit volume corresponding to the dynamically loaded SF and IPC samples are shown in Fig. 6.11. The cumulative energies absorbed per unit volume for both the SF and IPC samples follow a nearly linear trend beyond yielding. Also, as seen

from the graphs, the energies absorbed by lower V_f samples are consistently higher than that absorbed by higher V_f samples throughout the loading history.

(a)   (b)
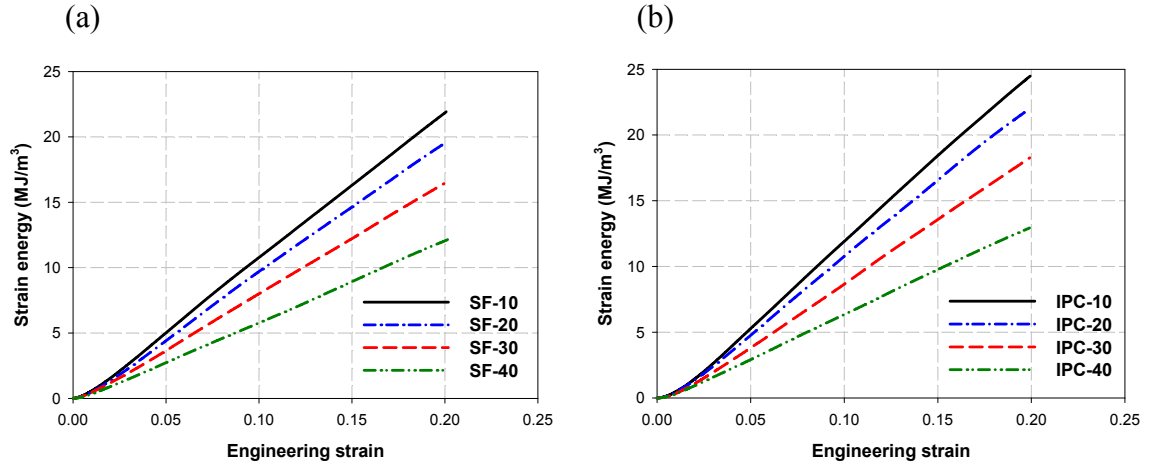
Figure 6.11: Strain energy absorption history of (a) SF and (b) IPC

with increasing strain in SHPB tests

6.4 Failure progression

Another interesting outcome under dynamic loading conditions is strain recovery in SF and IPC foam samples. The final lengths of the deformed samples were measured after experiments on both SF and IPC. Interestingly, for SF samples, the final measured lengths were more than that predicted by the SHPB equations after imposing a 25% engineering strain. This suggests that the SF samples had partially recovered (sprung-back) after the loading pulse had ended. Although the source/s of spring-back in SF is/are unclear at this point and would be interesting to study in the future, this phenomenon was negligible in the case of IPC samples. Whatever caused the spring-back to occur in the SF, is probably overcome in the IPC by the aluminum ligaments. Once aluminum ligaments undergo plastic deformation, they prevent the SF from springing-back. This

aspect of SF relative to IPC needs to be considered in an application if spring-back is a design factor.

This issue was further examined optically by tracking the progression of deformation under static and dynamic loading conditions for both SF and IPC foams. To understand the failure of SF and IPC foams including the above noted spring-back behavior in SF, real-time photography of progression of deformation during loading was carried out. The schematic of the experimental setup is shown in Fig. 6.12. This was also particularly important under dynamic loading conditions to assess progressive (failure originating at the impact end and propagating along the length of the bar) vs. steady-state deformation as stress waves propagate and deform the sample.
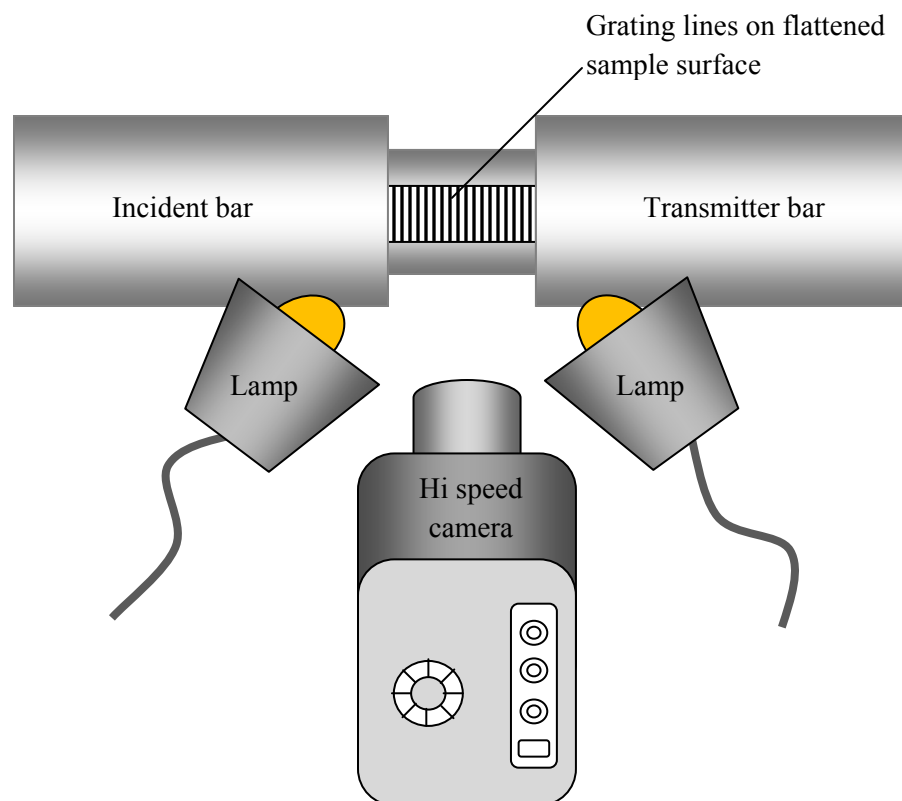
Figure 6.12: Schematic of the experimental setup used for high-speed photography to study real-time failure progression in SF and IPC samples in the SHPB set up

Two narrow (3 mm wide) diametrically opposite flat surfaces were machined on the foam samples and were printed with a line grating (pitch = 0.4 mm). The grating lines were first drafted using Solid Edge[TM] software and then printed on a decal paper. The printed grating lines on the decal paper were then transferred to the specimen surface. A few selected photographs of the specimen with gratings recorded using digital high-speed photography (186,000 frames/sec) are shown in Fig. 6.13.

9.5 mm

(a) t = 0 μs, l = 9.53 mm   (b) t = 72 μs, l = 8.1 mm   (c) t = 135 μs, l = 7.4 mm

(d) t = 197 μs, l = 7.6 mm   (e) t = 350 μs, l = 7.8 mm   (f) t = 850 μs, l = 8.1 mm

Figure 6.13: Stages of dynamic deformation of SF-30. Images (a)-(c) correspond to the first loading pulse and (d)-(f) correspond to later time instants showing presence of spring-back. The pitch of the coarse grating lines is 0.4 mm. The sample was loaded in the horizontal direction; $t = 0$ corresponds to the time when deformation begins.

The image in Fig. 6.13(a) corresponds to the undeformed sample just before the onset of the loading pulse in SHPB. The subsequent images show the deformed samples at different time instants (t). It is evident from the deformed length (l) that there was continuous decrease in the sample length up to 135 μs. This time instant is also when the loading pulse starts to decay due to the finite striker length. That is, $t = 135$ μs marks the end of the constant strain rate region of the loading pulse. The approximate strain at 135 μs calculated directly from the image is ~23% which is close to the obtained engineering strain of 22% using SHPB equations. Around 195 μs the sample starts to spring-back. At the 850th μs the sample has regained about 0.7 mm in length which is about 9.5% of the deformed length at the end of the loading pulse at 135 μs. Figures 6.13(d), (e) and (f) correspond to time instants after the end of the first incident stress wave, and before the second incident stress wave.

From the images shown in Fig. 6.13, due to the coarseness of the gratings used, shear bands seen on the specimen surface in Fig. 6.6(a) are not readily evident although a hint of these bands can be visualized in Fig. 6.13(c) and beyond. Much higher gratings densities and magnification are needed to achieve the necessary spatial and temporal resolutions in this regard. To contrast the response of SF with that of IPC, a similar optical observation using high-speed photography was also carried out for an IPC sample. A selection of corresponding real-time images is shown in Fig. 6.14. Noticeably, the quality of the images in these experiments is not as good as the ones in Fig. 6.13 due to the presence of shiny aluminum ligaments in the IPC which perturb the overall light field making it difficult to image the specimen. Nevertheless, qualitative observations regarding the nature of deformation progression can be made. The spring-back

phenomenon seen in SF is nearly absent in IPC samples under stress wave loading as evident from Figs. 6.14 (d), (e) and (f).

(a) t = 0 µs, l = 9.53 mm   (b) t = 72 µs, l = 8.97 mm   (c) t = 133 µs, l = 7.85 mm

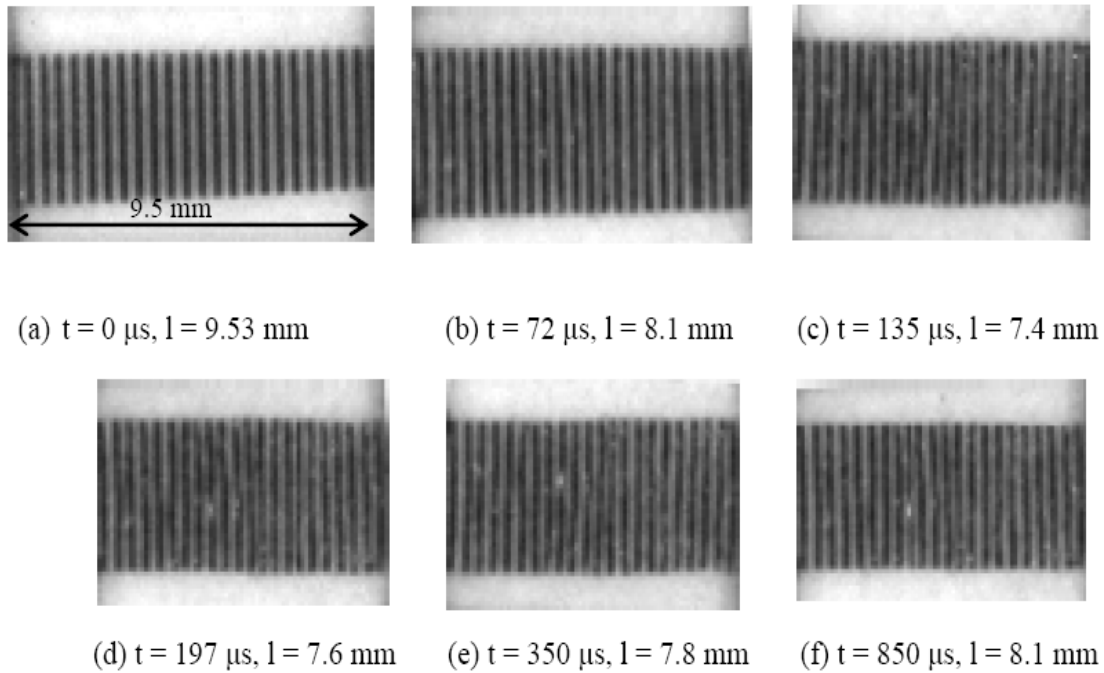(d) t = 200 µs, l = 7.85 mm   (e) t = 350 µs, l = 7.98 mm   (f) t = 850 µs, l = 7.98 mm
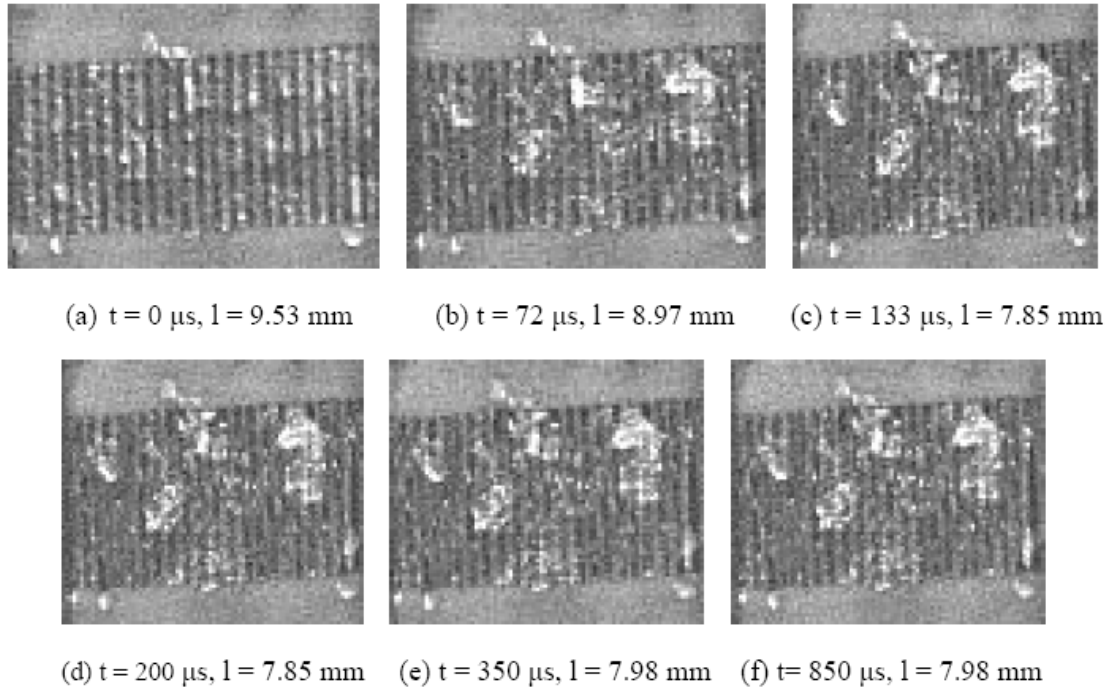
Figure 6.14: Stages of dynamic deformation of IPC-30. Images (a)-(c) correspond to the first loading pulse and (d)-(f) correspond to later time instants showing absence of spring-back. The pitch of the coarse grating lines is 0.4 mm. The sample was loaded in the horizontal direction; t=0 corresponds to the time when deformation begins.

7 FINITE ELEMENT MODELING AND ANALYSIS OF IPC FOAM

In view of the geometric complexity of modeling the IPC foam computationally, a unit-cell analysis was undertaken. A single cell of the IPC foam was used to predict the dynamic compressive response. The geometry was modeled using solid modeling software Solid Edge and imported into the finite element analysis software ABAQUS/Explicit. In ABAQUS, the dynamic/explicit algorithm was chosen to solve the temporal deformation process numerically. The following details the methodology adopted for geometric modeling and finite element analysis.

7.1 Geometric modeling

In 2005, Gong *et. al*., [38] studied the compressive response of unfilled open-cell foams. In their work, they reported that the number of sides of a cell range from 9 to 17, the average being 13.7 (see, insert in Fig. 3.1(b)). Accordingly, they chose a 14 sided polyhedron (tetrakaidecahedron) [39] called a Kelvin cell to represent a single cell of the open-cell foam in their analysis. In this research, the same Kelvin cell was adopted as an idealized representation of a unit-cell of the aluminum open-cell foam. The polyhedron consists of 6 squares and 8 hexagons, with all the edges having the same length l, as shown in Fig. 7.1. The height, h of the Kelvin cell is $h = 2\sqrt{2}l$ [38]. The length of the ligaments in the actual aluminum foam was ~1.5 mm and the same dimension was

chosen for the ligaments in the idealized model. The resulting wire mesh of the Kelvin cell model had a height, $h \sim 4.24$ mm. Further, the Kelvin cell was modeled as a solid with triangular cross section ligaments based on the actual cross sectional shape of the aluminum ligaments, increasing the total height of the model to ~ 4.69 mm. The cross section of the ligaments was chosen to be an equilateral triangle with ~ 0.78 mm sides for reasons to be discussed shortly. In reality, the cross section along the actual ligaments was not a constant, but considering the complexity of geometric modeling, the ligaments were modeled as having a constant cross sectional dimension.

3D array of Kelvin cells   Unit cell IPC   Ligament

4.69 mm

1.5 mm

Side view of unit cell IPC
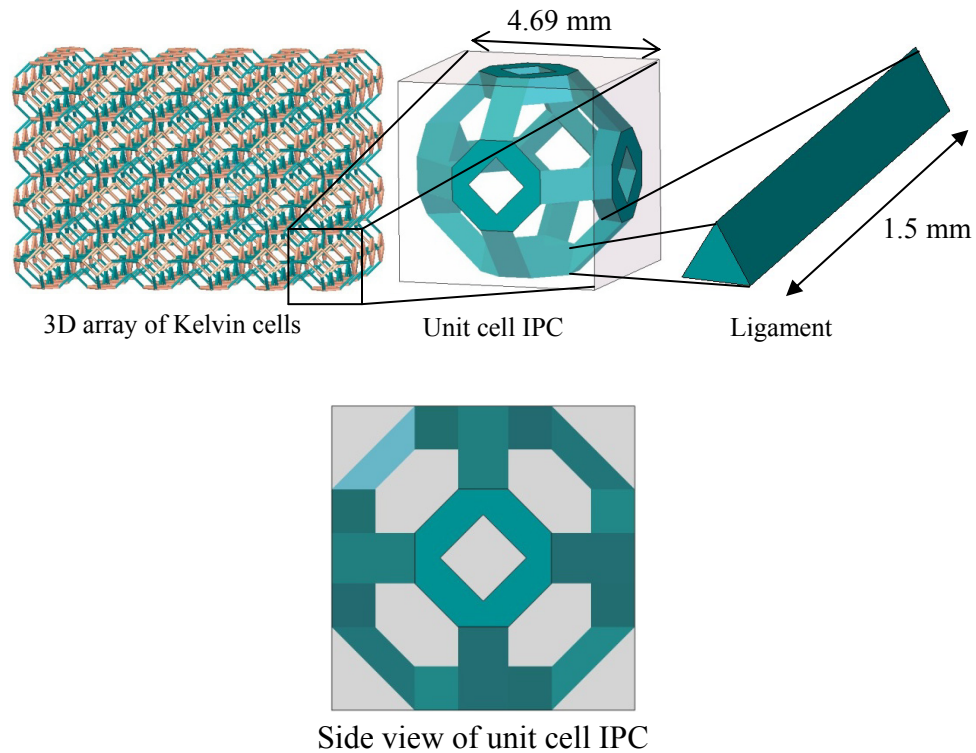
Figure 7.1: Schematics representing the building blocks of an idealized

Kelvin cell based IPC

Though there are some non conformances of the model geometry to the actual geometry, the aluminum volume fraction in the model matches the volume fraction range (8 -10% as claimed by the manufacturer of the aluminum foam) of the aluminum in the actual test sample. Thus, the resulting IPC model had an overall dimension of ~ 4.69 mm x 4.69 mm x 4.69 mm. The region not occupied by aluminum was "filled" with the SF material. In Fig. 7.1, the periodic arrangement of the Kelvin cells in 3D space resulted in a regular, well organized idealized open-cell foam whereas in actual aluminum foam, the cells are not periodic. Nevertheless, the randomness of the actual aluminum foam cells were assumed to be uniform on the scale of the test sample dimensions.

7.2 Computational model

7.2.1   Material properties

The material definitions for the SF region were assigned the compressive material properties of the respective microballoon volume fraction SF obtained from the SHPB experiments (Chapter 6). The elastic moduli were obtained by computing the slopes of the stress-strain curves obtained from the SHPB experiments. The Poisson's ratios and the density of the SF are shown in Table 7.1. The aluminum region was assigned a bilinear stress strain property corresponding to Al 6101 based on Alcoa Inc. datasheet[1]. The elastic regime for aluminum was assigned a Young's modulus of 69 GPa and a Poisson's ratio of 0.35. The plastic regime was assigned an initial yield stress of 172 MPa at a plastic strain of 0, and a stress of 200 MPa at a plastic strain of 0.148, for Al 6101 as shown in Table 7.2.

---

[1] The metallic phase of the IPC was assumed to be strain rate independent.

Material	Elastic Modulus (MPa)	Poisson ratio	Density (kg/m^3)
Al 6101	69000	0.35	2700
SF-10	5122	0.34	995
SF-20	4529	0.34	870
SF-30	4459	0.34	796
SF-40	3835	0.34	696

Table 7.1: Elastic properties of SF and aluminum used in the finite element model

Plastic strain	Stress (MPa)
0	172
0.148	200

Table 7.2: Inelastic properties of Al 6101 used in the finite element model

7.2.2 Yielding and hardening

The von-Mises yield criterion was used to define material yielding. Further, yielding was assumed to be isotropic. This criterion uses the equivalent uniaxial plastic strain and the corresponding uniaxial stress input to define the yield surface [40, 41]. The material property input for the plastic regime was supplied in the form of stress as a tabular function [40] of plastic strain. In ABAQUS, the stress at any given state within the maximum plastic strain defined will be interpolated [40] based on the supplied tabular

data. Beyond the maximum plastic strain defined, the stress remains constant and equal to the stress value in the previous step in the data [40]. The hardening and softening behaviors are also assumed to be isotropic. This means that the yield surface is the same [40] in all directions based on increasing or decreasing stress as plastic straining occurs. In the current material system, aluminum could be undergoing strain hardening, while the SF could be softening. The yield function [41] for isotropic hardening is expressed as,

$$f(\sigma) = \sigma^0(\varepsilon^{pl}, \theta)$$

where σ^0 is the equivalent uniaxial stress, ε^{pl} is the equivalent plastic strain and θ is temperature. Reference [41] details the algorithm that ABAQUS uses to solve the nonlinear material model based on the von-Mises yield criterion. Some of the details are as follows:

The total strain can be partitioned into elastic and plastic strains as,

$$\varepsilon = \varepsilon^{el} + \varepsilon^{pl} \tag{7.1}$$

where ε is the total strain and ε^{el} and ε^{pl} are the elastic and plastic strain components, respectively. For a given stress state, the strain states could be different depending on the loading path. Due to this, increments of plastic strain (de^{pl}) need to be computed based on the loading path before obtaining the total strain for a particular state of stress [42]. The Prandtl-Reuss plasticity relations state that the increments of plastic strain depend only on the instantaneous deviatoric stresses [42]. Hence, the deviatoric stress matrix, S is obtained using

$$S = \sigma + pI \tag{7.2}$$

where σ is the stress matrix, I is the identity matrix and p is the volumetric stress given by

$$p = -\frac{1}{3} trace(\boldsymbol{\sigma}). \tag{7.3}$$

Further, p and $\boldsymbol{S}$ are related to strains under elastic conditions as

$$p = -K\varepsilon_{vol} \quad \text{and} \quad \boldsymbol{S} = 2G\boldsymbol{e}^{el}, \tag{7.4}$$

where, K and G denote the bulk modulus and shear modulus, respectively, ε_{vol} is the elastic volumetric strain, and $\boldsymbol{e}^{el}$ is the deviatoric elastic strain. It is to be noted that bold symbols $\boldsymbol{\sigma}, \boldsymbol{S}$ and $\boldsymbol{I}$ represent (3x3) matrices. Now, writing the incremental plastic strain as a product of its scalar value and its direction,

$$d\boldsymbol{e}^{pl} = d\bar{e}^{pl}\boldsymbol{n} ; \qquad \boldsymbol{n} = \frac{3}{2}\frac{\boldsymbol{S}}{q}, \quad q = \sqrt{\frac{3}{2}\boldsymbol{S}{:}\boldsymbol{S}} \tag{7.5}$$

where, $\boldsymbol{e}^{pl}$ is the deviatoric plastic strain, $\bar{e}^{pl}$ is the scalar deviatoric plastic strain, $\boldsymbol{n}$ is the direction vector and q is the estimated equivalent uniaxial stress. Equation (7.5) is called the integrated flow rule.

The above equations are then solved for the state of the material at the end of every increment. The state of the material refers to the estimated equivalent uniaxial stress (q) as a function of deviatoric equivalent plastic strain ($\boldsymbol{e}^{pl}$). The state of the material will be verified by checking if the estimated stress (q) equals the scalar equivalent stress ($\bar{\sigma}$) corresponding to the scalar deviatoric plastic strain ($\bar{e}^{pl}$) of that load step. It is understood that $\bar{\sigma}$ corresponding to a particular $\bar{e}^{pl}$ is obtained from the material definition input as stated at the beginning of this section. Therefore, the condition to be verified is,

$$q = \bar{\sigma}(\bar{e}^{pl}). \tag{7.6}$$

To check this condition, the expression for q would first be obtained as follows:

The change in the deviatoric plastic strain (Δe^{pl}) between the current and the previous increment is computed as

$$\Delta e^{pl} = \Delta \bar{e}^{pl} \boldsymbol{n} . \tag{7.7}$$

Using Eqs. (7.1) and (7.7), Eq. (7.2) is modified as

$$\boldsymbol{S} = 2G(e^{el}|_t + \Delta e - \Delta \bar{e}^{pl} \boldsymbol{n}) \tag{7.8}$$

where, $\Delta \boldsymbol{e}$ is the change in the total strain. In the above equation, the term in the parentheses is the estimated elastic strain value at the end of the current iteration. The subscript t represents the previous time step. Now, substituting for $\boldsymbol{n}$ in the above equation from Eq. (7.5),

$$\left(1 + \frac{3G}{q}\Delta \bar{e}^{pl}\right)\boldsymbol{S} = 2G\hat{\boldsymbol{e}} ; \qquad \hat{\boldsymbol{e}} = (e^{el}|_t + \Delta e). \tag{7.9}$$

The inner product of the above equation with itself gives

$$q + 3G\Delta \bar{e}^{pl} = 3G\tilde{e} ; \qquad \tilde{e} = \sqrt{\frac{2}{3}\hat{\boldsymbol{e}}:\hat{\boldsymbol{e}}} . \tag{7.10}$$

As q must now satisfy Eq. (7.6), the above equation is modified as

$$3G(\tilde{e} - \Delta \bar{e}^{pl}) - \bar{\sigma} = 0. \tag{7.11}$$

The above equation is then solved using Newton's method to get,

$$c^{pl} = \frac{3G(\tilde{e} - \Delta \bar{e}^{pl}) - \bar{\sigma}}{3G + H} ; \qquad H = \frac{d\bar{\sigma}}{d\bar{e}^{pl}} , \tag{7.12}$$

where, c^{pl} is the error in the plastic strain increment in case Eq. (7.6) is not satisfied. H is the strain hardening function, which is nothing but the relationship between the respective stresses and plastic strains given as the material definition input (in this work, the input is given in a tabular format). Now, the new $\Delta \bar{e}^{pl}$ or the new plastic strain increment value for the next iteration for the same load step is obtained as

$$\Delta \bar{e}^{pl} = \Delta \bar{e}^{pl} + c^{pl}. \tag{7.13}$$

The iteration is then carried out until $\Delta\bar{e}^{pl}$ converges, or until c^{pl} approaches zero. At this stage, the solution for that increment is fully defined. The converged change in scalar equivalent plastic strain ($\Delta\bar{e}^{pl}$) is used in Eq. (7.9) to obtain the deviatoric stress (S) that corresponds to the equilibrium state for that particular increment. The volumetric stress (p) is also now computed using Eq. (7.3).

In essence, for each increment of load, the deviatoric and volumetric stresses corresponding to the equilibrium states are computed based on the converged value of change in the scalar equivalent plastic strain at every integration point in the model.

7.2.3   Explicit integration scheme in ABAQUS

The explicit central difference integration rule is used to solve the equations of motion governing a dynamic event in ABAQUS. The implementation of this rule in ABAQUS [40] is summarized in the following:

At the beginning of every increment, t, the explicit central difference operator satisfies the dynamic equilibrium equations; the result of which is the acceleration at that time step,

$$\ddot{u}_{(i)} = (M)^{-1}\left(P_{(i)} - I_i\right) \tag{7.14}$$

where $\ddot{u}_{(i)}$ represents the acceleration with u as the degree of freedom, the subscript i is the increment in an explicit dynamic step, M is the mass matrix, P is the applied load vector and I is the internal force vector. The velocity for the time $t + \frac{\Delta t}{2}$ is computed using the acceleration at time t. Then, using this computed velocity and the displacement at time t, the displacement at time $t + \Delta t$ is computed as, [40]:

$$\dot{u}_{\left(i+\frac{1}{2}\right)} = \dot{u}_{\left(i-\frac{1}{2}\right)} + \frac{\Delta t_{(i+1)} + \Delta t_{(i)}}{2}\ddot{u}_{(i)} \tag{7.15}$$

and

$$u_{(i+1)} = u_{(i)} + \Delta t_{(i+1)} \dot{u}_{\left(i+\frac{1}{2}\right)} .$$ (7.16)

At time $t = 0$, the initial values of velocity and acceleration are set to zero, unless specified otherwise, and the mid-increments $\dot{u}_{\left(+\frac{1}{2}\right)}$ and $\dot{u}_{\left(-\frac{1}{2}\right)}$ are given as

$$\dot{u}_{\left(+\frac{1}{2}\right)} = \dot{u}_{(0)} + \frac{\Delta t_{(1)}}{2} \ddot{u}_{(0)}$$ (7.17)

and

$$\dot{u}_{\left(-\frac{1}{2}\right)} = \dot{u}_{(0)} - \frac{\Delta t_{(0)}}{2} \ddot{u}_{(0)},$$ (7.18)

respectively.

The displacements will then be used to obtain the state of the material as described above. Unlike the implicit scheme, iterations are not used here to achieve convergence. Instead, the stability of the solution is governed by the appropriate time step size (Δt), which is dictated by the time required by the stress wave to travel the smallest element and the maximum wave speed in the model defined [40]. The time step size should be chosen to be sufficiently small, typically a third or lower than the time taken by the stress wave to travel the smallest element in the mesh.

7.3 Discretization

The unit cell model of the IPC was used to predict the overall response of the test sample. The geometric model was imported into ABAQUS and discretized using four noded linear tetrahedron (C3D4) [40] elements. To check for the appropriateness of the mesh refinement, a model meshed with elements having 0.2 mm and 0.1 mm edge length were simulated and the stress vs. strain results corresponding to the two mesh sizes were

compared. The comparison (Fig. 8.2) shows that the results nearly overlap on each other. So, for all further analyses, the model was meshed with elements having an approximate element edge of length 0.2 mm.
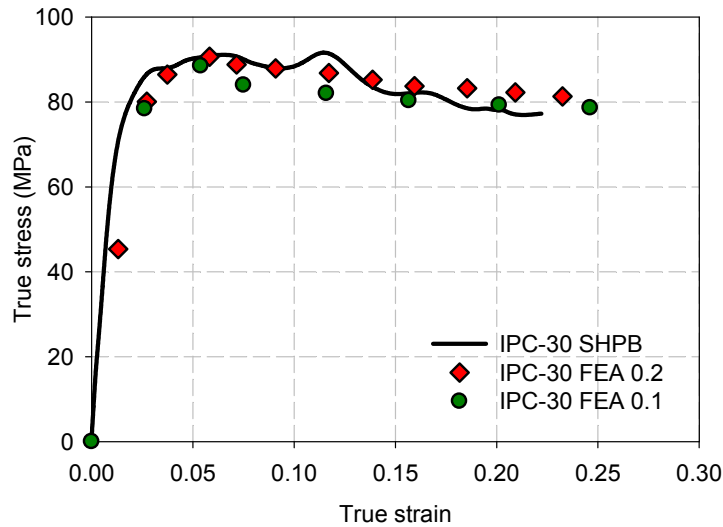
Figure 7.2: Check for appropriateness of discretization

In order that the model better represents the sample, the unit cell is imagined to be located deep within a large material volume. The Solid Edge model of the unit cell has exposed faces, and does not represent a cell within the material volume. This is because, in a dynamically loaded sample, the stress waves travel through the entire length of the sample before reflecting at the end of the sample, whereas in the model the stress waves would get reflected at the boundaries of the cell itself. To overcome this shortcoming, a skin / layer of SF and aluminum material was modeled adjacent to the corresponding material at the boundary of the cell. This skin was meshed using the so-called *infinite elements* [43].

Figure 7.3: Illustration showing (a) the infinite element layer in the FE model and stress

wave behavior in the (b) absence and (c) presence of infinite element layer

7.3.1 Infinite elements – Background

The infinite elements are used in situations where the region of analysis is very small compared to the region surrounding it [40]. One of the earliest and probably the most important work on infinite elements was carried out by Bettess [43]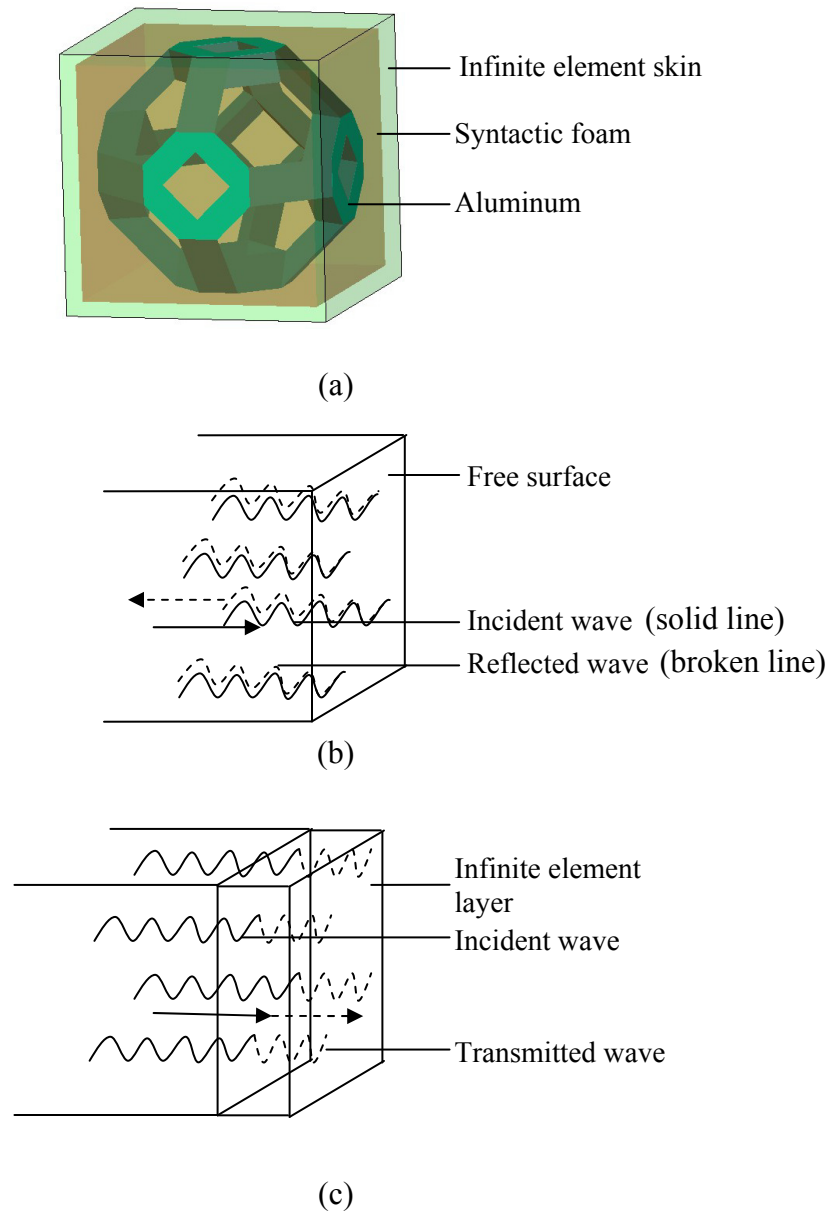 in 1977. He suggested Lagrange polynomial type shape functions that include an exponential decay term. Bettess states that the infinite elements should satisfy two main requirements, one that the shape functions should be realistic and the other that it should lead to integrations over the finite element domain. Accordingly, Bettess proposed shape functions for one dimensional domain presented as,

$$N_i = e^{(x_i-x)/L} \prod_{\substack{j=1 \\ j \neq i}}^{n-1} \left(\frac{x_j - x}{x_j - x_i} \right)$$

where, n is the number of points in the domain, x is the coordinate and N_i is defined for i varying from 1 to n-1 and $j \neq i$. Among all the points in the domain, the nth point is infinitely distant and all other points have finite x-coordinates. As reported by Bettess, in the above expression, L is an arbitrary distance and serves as the measure of severity of the exponential decay.

Since its inception, infinite elements have been developed and used by several researchers. In 1987, Haggblad and Nordgren [44] used infinite elements to model the far field regions to study a nonlinear soil-structure interaction effect. Viladkar *et al.* [45] also used infinite elements coupled with finite elements to idealize and study interactions between the far field soil regions and plane frames. Two types of infinite elements were developed and used by Park *et al.* [46] to analyze the hydrodynamic forces on offshore structures. One type was used to model radiation in the fluid at infinity and the other type

used to model the fictitious bottom boundary of the deep water. Later in 1993, Zhao and Valliappan [47] developed a 3D dynamic infinite element that satisfies four different requirements all of which are very useful in representing practical problems much more efficiently. Two of those requirements used in the FE model of the current work are, interfacial displacement compatibility between finite and infinite elements and displacement continuity at the common boundary between infinite elements possessing different material properties.

In ABAQUS, as infinite elements are associated with the far field regions, their behavior is assumed to be linear and the material response isotropic [40]. The particular infinite element used in this analysis is a 3D, 8 node, one-way infinite brick (CIN3D8) [40]. The infinite elements (CIN3D8) transmit any stress wave incident on them to a hypothetically infinite distance in one direction and thus prevent any reflection of stress waves at the boundary of the unit cell. This phenomenon made possible by the implementation of a layer of infinite elements in the finite element model enforces the condition that the unit cell is located within a larger volume of IPC material. Those infinite elements adjacent to aluminum were assigned the properties of aluminum, and those that are adjacent to SF were assigned the SF properties as seen in Fig. 7.4. Even though all the sides of the IPC have infinite element layers, for clarity purposes, the infinite element layer on only one side is shown in Fig. 7.4.

7.4 Boundary conditions and loading

The unit cell is supported on the free surface of the infinite element layer on one side. On the side opposite to that of the support, and on the surface of the unit cell which

marks the boundary between the unit cell IPC and the infinite element layer, a velocity pulse of magnitude 10250 mm/s for a time period of 250 microseconds is applied. This velocity corresponds to the approximate particle velocity in the incident bar at the incident bar / sample interface. The particle velocity (V_{PI}) in the incident bar is given by,

$$V_{PI} = C_{bar} \times \epsilon_{bar} = 5.123 \times 10^6 \, mm/s \times 0.002 \cong 10250 \, mm/s,$$

where C_{bar} is the incident bar wave speed and ϵ_{bar} (~ 0.002) is the maximum plateau strain in the incident bar caused by the stress wave. The time period of 250 microseconds was chosen as it is the approximate duration for which the actual test samples were loaded in the SHPB experiments.
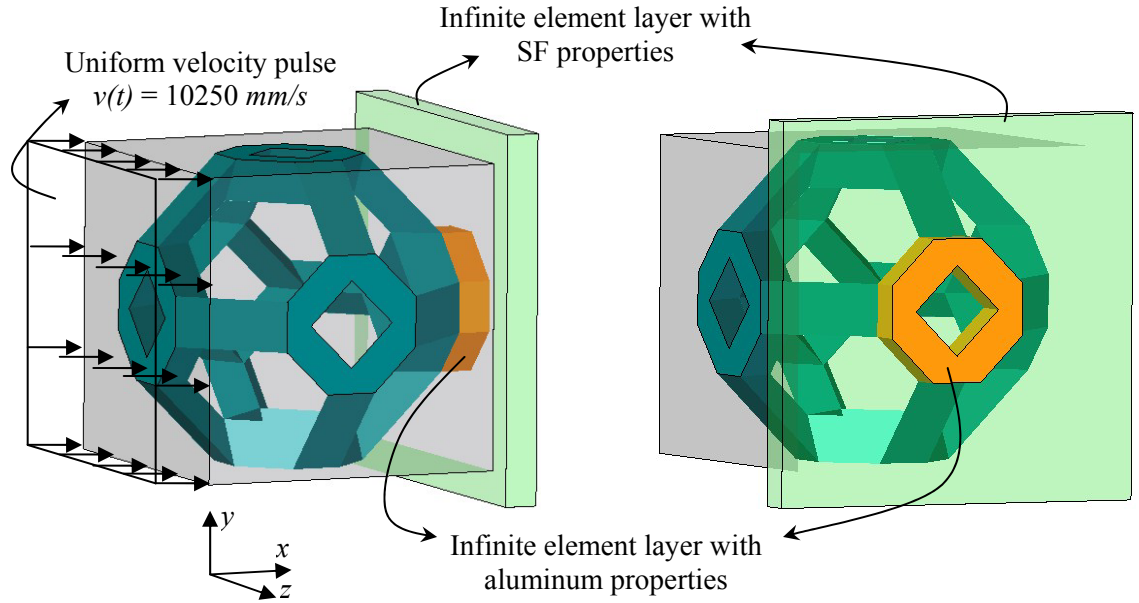

Figure 7.4: Load and boundary conditions

7.5 Other analysis parameters

The analysis was set up to simulate the dynamic problem for 250 microseconds, same as the loading pulse duration. The load steps were automatically selected by the ABAQUS software based on the fastest wave speed and the smallest element size in the model [40]. The load step period is chosen to be less than the time taken by the stress wave to traverse the smallest element in the model. As a verification procedure, the software checks if the deformation speed of the material is less than one-third the wave speed in the material at each load step. As large deformations were expected during the deformation, geometrical nonlinearity effects were also included in the analysis procedure.

7.6 Results from finite element analysis

7.6.1 Stress-strain response

The stress and strain histories of all the elements (aluminum and SF) on the surface of the cell on the side directly opposite to the loaded surface were obtained. From the data obtained, the average stress and strain histories were obtained, which were used to plot the dynamic stress-strain curves. The same procedure was followed for all the numerical IPC models corresponding to 10%, 20%, 30% and 40% microballoon volume fractions in SF, and the results are shown in Fig. 7.5. The trends are similar to those observed from the experimental results discussed in Ch. 6, Fig. 6.7.
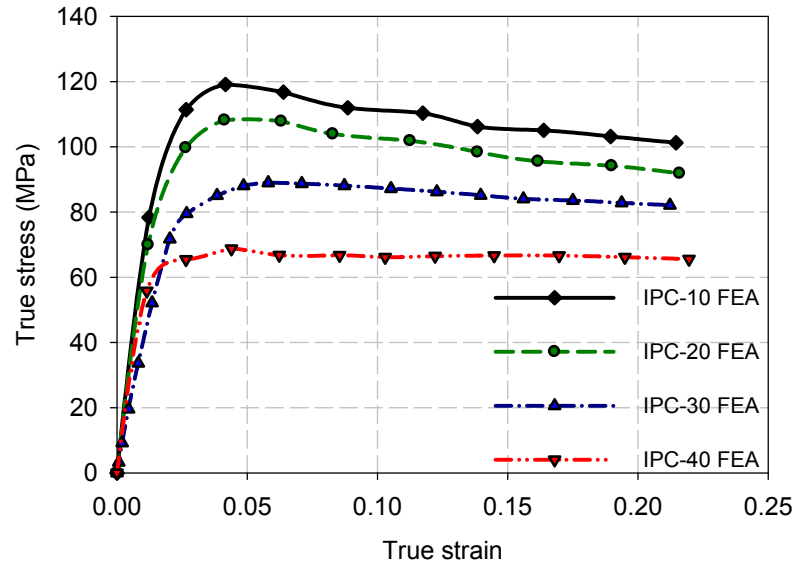
Figure 7.5: True stress – true strain responses of different IPC obtained

from finite element analysis

7.6.2 Comparison between experimental and finite element results

The graphs in Fig. 7.6 show the dynamic stress-strain responses of all volume fraction IPC models obtained from the finite element analysis. In general, a good agreement between the measured results and finite element results is observed. The differences between the experimental results and the simulations are attributed to the following issues:

- In the actual specimens micro cracking occurs whereas the numerical model does not allow any debonding to occur at material interfaces.

71

- The material property of aluminum used in the model corresponds to the quasi-static compressive response. This assumption was used considering the fact that aluminum is relatively strain rate independent.

- The infinite elements transmit all the stress waves that are incident on them. In the real situation however, there will be stress wave reflections back into the sample at the sample / transmitter bar interface within the duration of 250 microseconds.
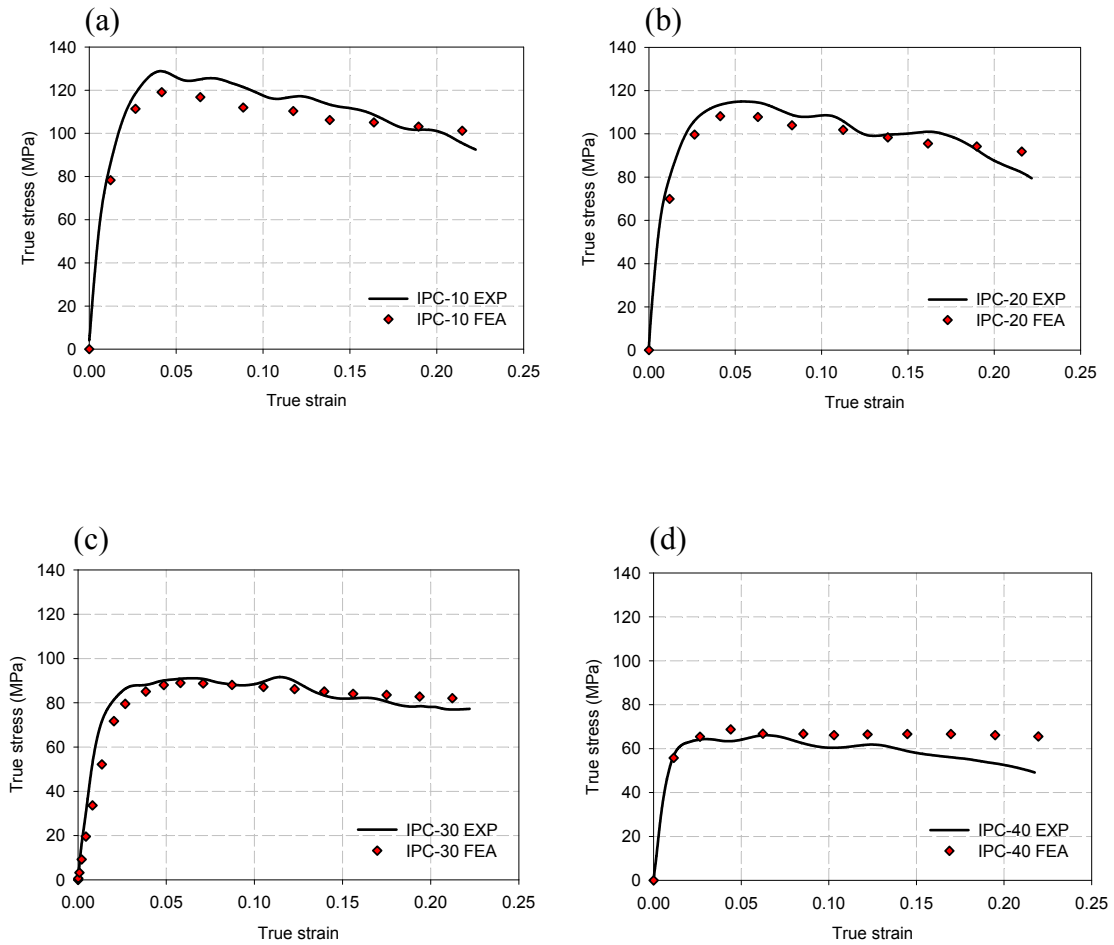

Figure 7.6: Comparison of experimental and FEA results of (a) IPC-10, (b) IPC-20, (c) IPC-30 and (d) IPC-40

7.6.3 Analysis of contour plots

From the finite element analysis, the von-Mises stresses, the equivalent plastic strains, displacements along the loading direction, the kinetic energy and the total strain energy of the whole model for up to 22% true strain were obtained. To appreciate the spatial and temporal distribution of these quantities in a dynamically deforming IPC, the FE results (contour plots) corresponding to the IPC-30 model is presented. In these contour plots, the left hand side images show contours on the outer surface of the IPC. The right hand side images show contours on the *x*-y plane of the section made at exactly half the length of the unit cell along the *z*-direction. From the stress contour plots (Fig. 7.7), it can be seen that the aluminum ligaments experience the maximum stress, approximately 200 MPa, equal to the yield stress of aluminum. The maximum stress attained by the SF however is approximately 70 MPa, which is close to the yield stress of SF-30 obtained from the experiments. From the figures, it is also evident that the stress concentrations occur in the vicinity of the ligament joints. This is expected considering the geometry and the material discontinuity present in the model.

(a) 5% strain
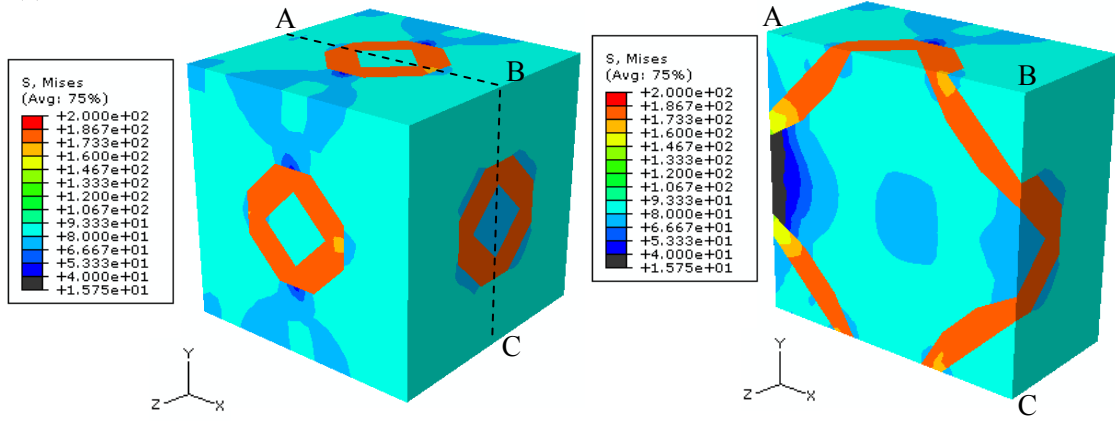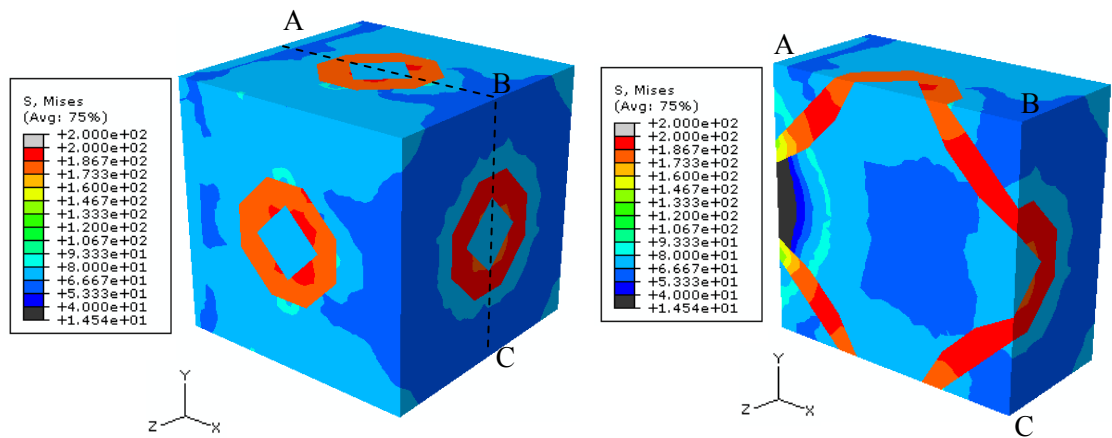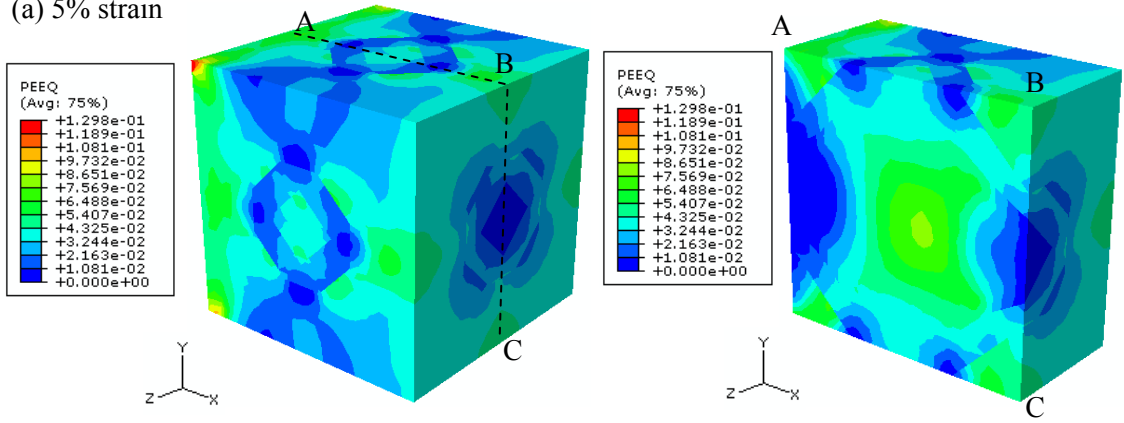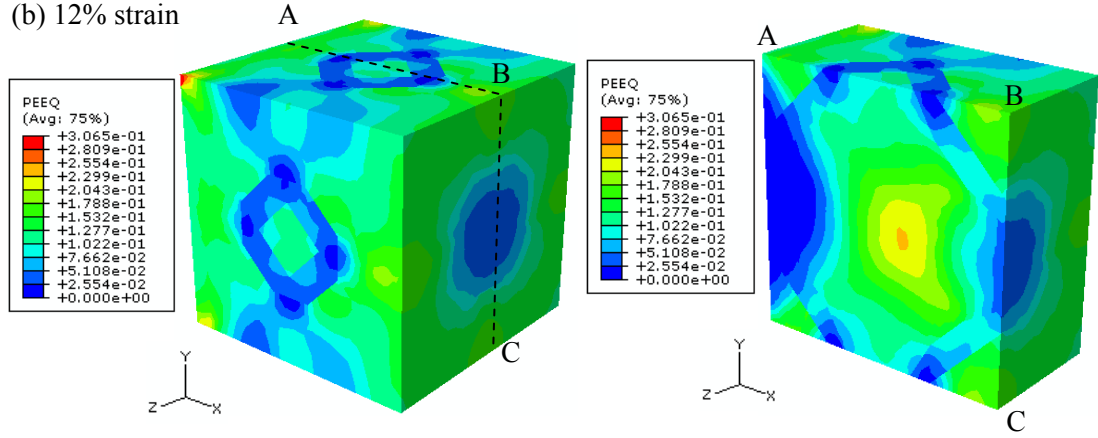
(b) 12% strain
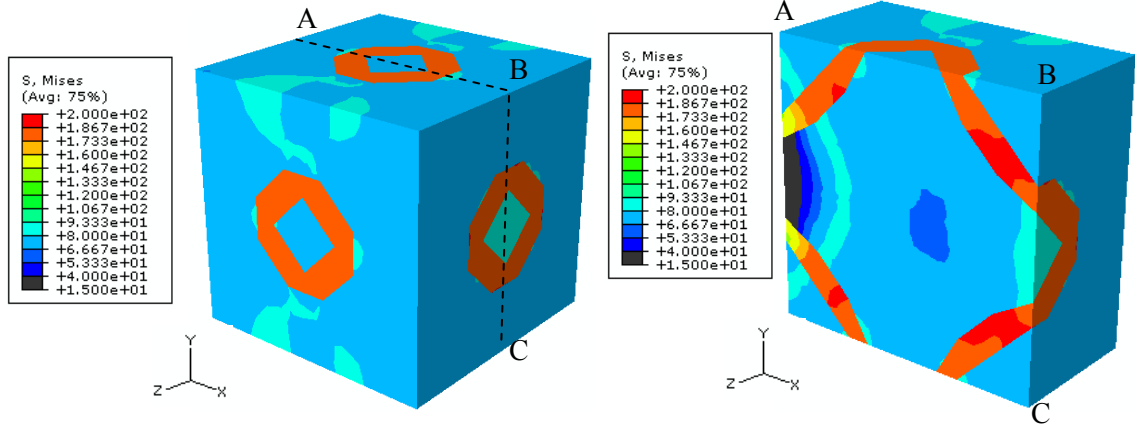
(c) 20% strain

Figure 7.7: Mises stress contour plots from dynamic FE model for IPC-30
Left side images: whole IPC, Right side images: sectioned IPC
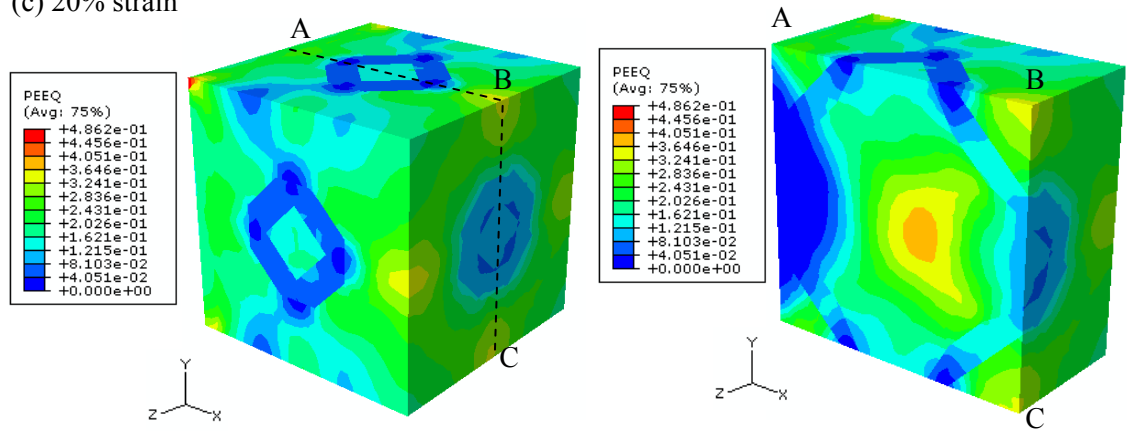(Loading is along the *x*-direction)

Figure 7.8: Equivalent plastic strain contour plots from dynamic FE model for IPC-30

Left side images: whole IPC, Right side images: sectioned IPC

(Loading is along the *x*-direction)

The contour plots of the equivalent plastic strain are shown in Fig. 7.8. From the contour plots, it is obvious that the SF regions have experienced larger plastic strains compared to that in aluminum. A much more interesting observation from the figures is that the locations of localized maximum plastic strain are not too close to the ligament joints. This suggests that very close to the ligament joints, the stiffer aluminum regions with low plastic strain have restrained the SF from deforming as much as the SF regions that are further away. The contours also help in appreciating the percentage of strain energy absorbed by the aluminum and the SF regions.

Unlike the stress contours and equivalent plastic strain contours, the displacement contours are rather continuous (Fig. 7.9). This is expected as debonding between the aluminum and SF regions are not allowed to occur in the model. That is, the material interfaces are modeled as perfectly bonded. The contours on the cross-section view reveal that up to half the length of the unit cell from the loading end the displacement at the center is more than that at the periphery. Beyond the mid-section of the cell, this trend is reversed. That is, the displacement is a maximum at the periphery and gradually decreases towards the center symmetrically. Near the mid-section, the displacement is nearly constant along the cross section.

(a) 5% strain
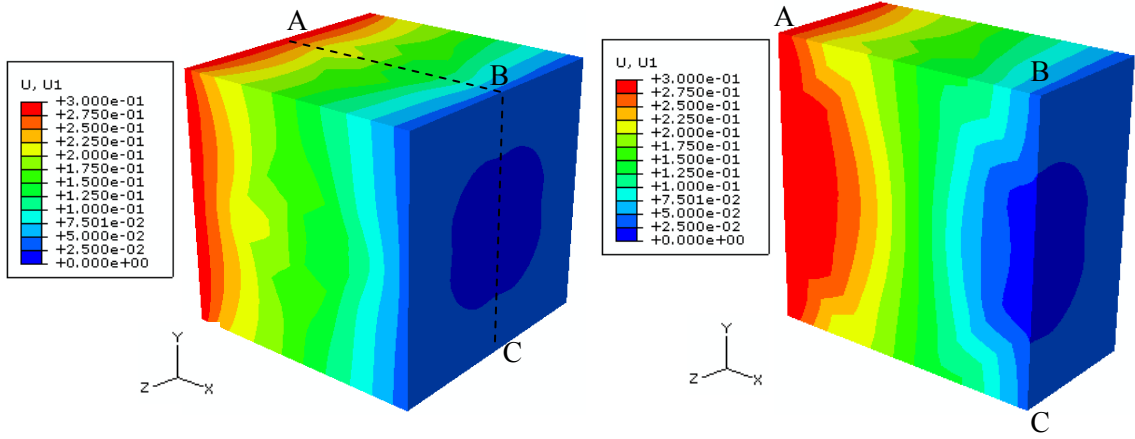
(b) 12% strain

(c) 20% strain
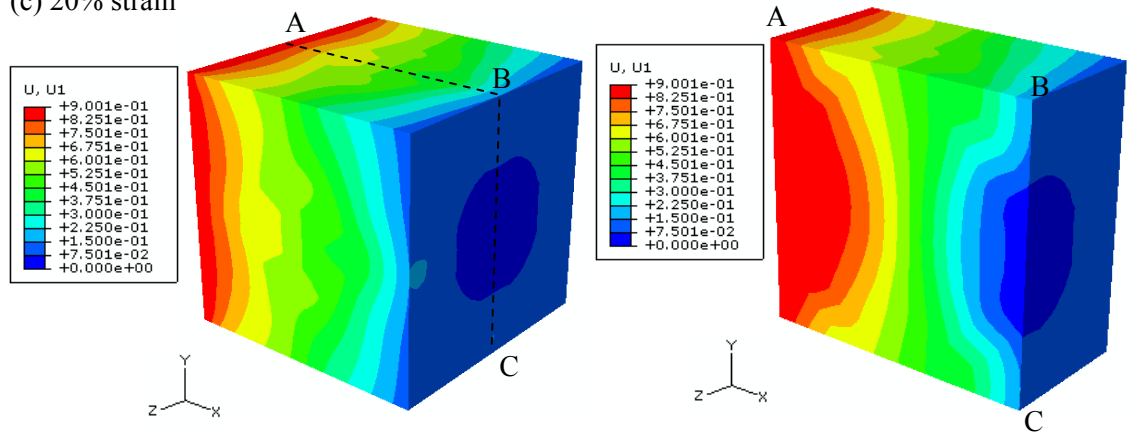
Figure 7.9: *x*-displacement contour plots from dynamic FE model for IPC-30

Left side images: whole IPC, Right side images: sectioned IPC
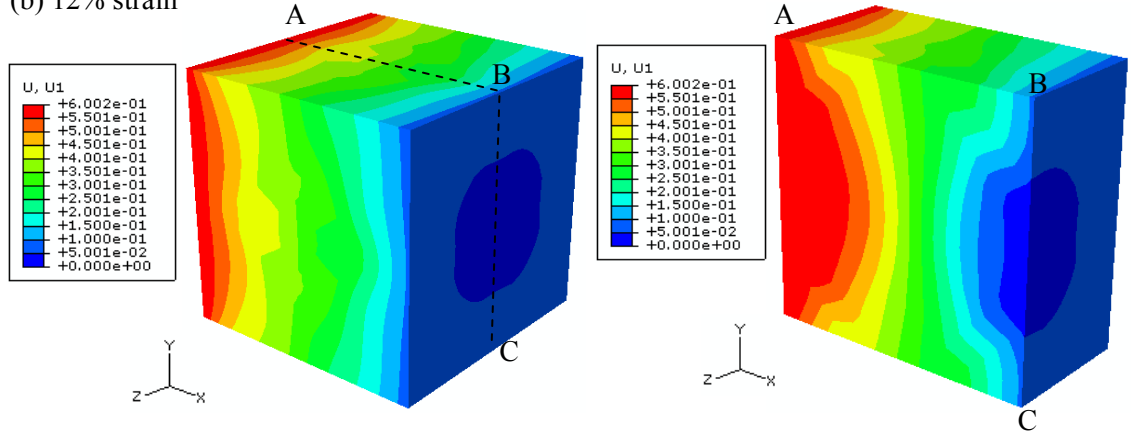
(Loading is along the *x*-direction)

7.6.4 Energy absorption

It was shown earlier (see Section 6.2.2) that the compressive strengths and the stresses beyond yield point in IPC are higher than their corresponding pure syntactic foam. In other words, the area under the stress-strain curve (or the energy absorbed per unit volume) for a dynamically deforming IPC is greater than that for a SF. The introduction of aluminum into the SF has helped enhance this property among others such as the compressive strength. At this stage it was thought to be a worthwhile effort to analyze the proportion of various energies absorbed by the aluminum and SF phases in the IPC. The kinetic energy (KE) trends and the total strain energy (SE) trends are of particular interest. Previously, the equivalent plastic strain contours gave a hint regarding the proportion of strain energy absorbed by the two phases of the composite foam. To quantify the proportions shared between the SF and the aluminum phases, the KE history and the SE history for a duration of 125 microseconds, which approximately corresponds to the 22% strain, are plotted below.
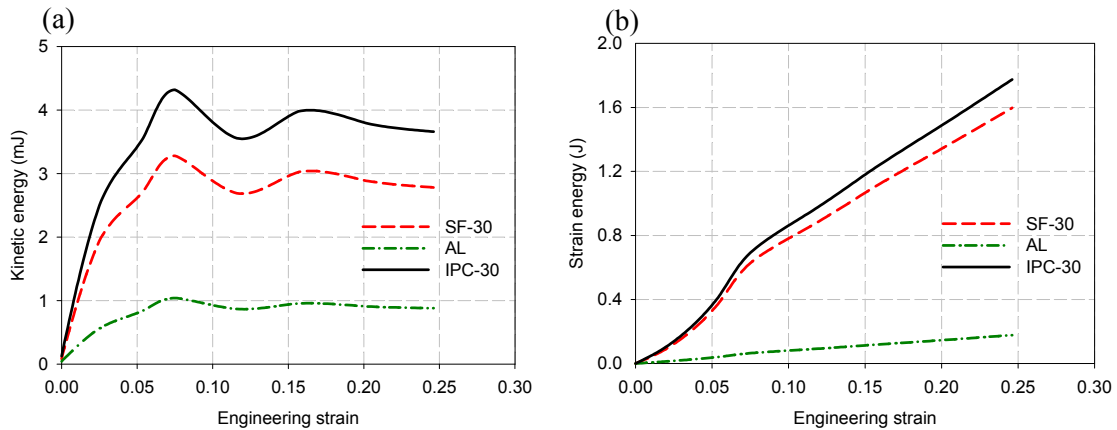
Figure 7.10: History of (a) kinetic energy and (b) strain energy absorption by aluminum and SF in unit-cell IPC-30

Figures 7.10(a) and (b) show the amount of KE and SE absorption by SF and aluminum per unit cell of IPC. To quantify the proportion of these two energies shared by SF and aluminum, the percentage of KE and SE absorbed by SF and aluminum per cell is plotted in Figs., 7.11(a) and (b), respectively. From the Fig. 7.11(a), it can clearly be seen that the KE absorbed by the aluminum region accounts for more than 20% of the total KE absorbed by the IPC throughout the loading history. It should be realized that the volume fraction of aluminum in the model IPC is ~8 %. So, 8% of the IPC material absorbs at least 20% of the total KE.
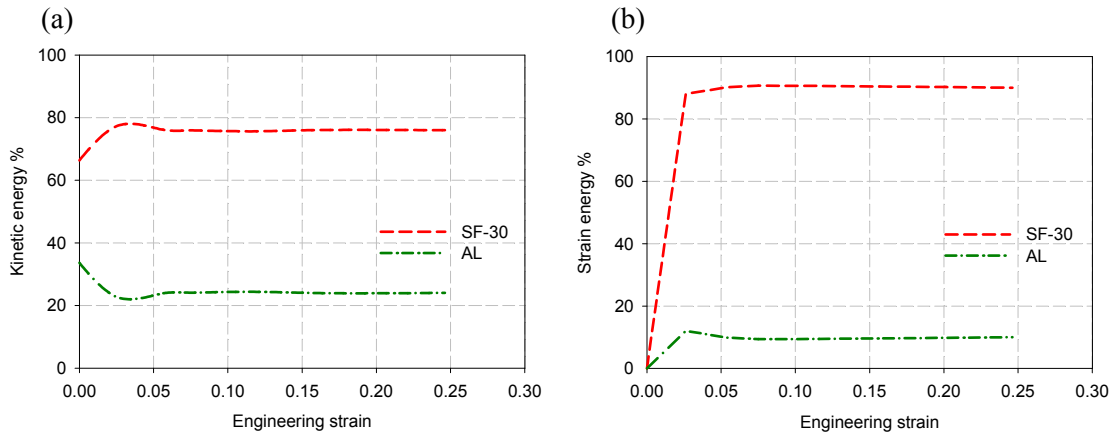
Figure 7.11: History of percentage of (a) kinetic energy and (b) strain energy absorption by SF and aluminum in IPC-30

From Fig. 7.11(b), it is seen that about 11% of the total SE is absorbed by aluminum during most of the loading history. Again, comparing the proportion of the SE absorbed by aluminum (~11%) to that of the volume fraction of aluminum in the model IPC (~8%), there is an encouraging, though not very prominent trend. The difference in KE and SE magnitudes (SE >> KE) is to be noted here. Although, the strain energy absorbed per unit cell (Fig. 7.11 (b)) by the aluminum region is considerably lower with

respect to that by the SF, the fact that aluminum comprises only ~ 8% of the total volume of the IPC cell makes the energy absorbed by the aluminum phase more significant. This suggests that if the aluminum phase is replaced with a more compliant material, the energy absorption by the resulting IPC might be higher than that observed in the aluminum foam / SF IPC. It should also be noted that using a more compliant material might prove to be detrimental to the overall structural integrity of the IPC. Nevertheless, the proposed FE model could be effectively used to predict the energy absorption characteristics of different material combinations.

8   SUMMARY

A split Hopkinson pressure bar was developed for characterizing the compression response of low impedance materials. The apparatus was successfully calibrated against compression data in the literature for acrylics at strain rates of 1250 /sec. The repeatability of stress-strain responses was demonstrated for different stress pulse durations as well as modest variations in pulse shapers.

Using this SHPB apparatus, the compression characteristics of Interpenetrating Phase Composite (IPC) foams were studied. The IPC foams were prepared by infusing uncured epoxy-based syntactic foam (SF) into open-cell aluminum preforms/scaffolds. Curing of SF resulted in an IPC structural foam with a 3D interconnectivity. The dynamic compression responses of IPC foams made of SF with 10% - 40% V_f of hollow glass microballoons were studied at strain rates of ~1500/sec. The responses of IPC foams were also evaluated relative to their pure SF counterparts. The failure progression in both types of samples was recorded using high-speed photography to examine the real-time deformation and failure processes. The micrographs were also used to explain the underlying failure mechanisms.

A unit-cell based finite element model of an IPC was developed using a Kelvin cell representation of aluminum ligaments of the open-cell scaffold. The dynamic compression response was simulated using ABAQUS structural analysis software. The

3D geometries for the SF and aluminum regions of the unit cell were modeled using Solid Edge. Elasto-plastic experimental measurements were used as the material property inputs for the SF region in the finite element IPC model. Infinite elements were used to model the external surface boundary of the unit-cell to idealize its presence within a large volume of the material.

The major conclusions of this work are as follows:

- The V_f of microballoons in SF plays a dominant role in the overall response of the SF and IPC foams. A monotonic increase in elastic modulus, yield stress, and plateau stress are evident as V_f of microballoons decreases. The IPC foams consistently have higher values for each of these characteristics relative to the corresponding SF.

- Unlike static results, under dynamic conditions SF and IPC samples show a stress-strain response that has only two dominant regimes – an initial proportional loading zone up to a maximum stress, and a subsequent monotonically softening zone. The foams with lower V_f of microballoons tend to soften more rapidly than the ones with higher V_f. The elastic modulus and maximum stress increase with decreasing V_f of microballoons under high-strain rate loading. The values for IPC are again higher than those for SF under dynamic conditions. The dynamic maximum stress values are also higher for both SF and IPC relative to the quasi-static ones.

- The dynamic energy absorption values ($U_{0.22}$) up to 22% strain are nearly twice the corresponding static values for both IPC and SF samples. The energy absorbed per unit volume by the IPC under dynamic conditions is about ~10% higher than the SF counterparts. The energy absorbed per unit mass, however, favors SF under dynamic conditions. This is unlike the observation under static conditions.

- The energy absorbed per unit mass for both the SF and IPC foams under dynamic loading follow a linear trend with respect to the applied strain.

- The failure of SF and IPC under dynamic conditions is dominated by the formation of an extensive network of shear bands in SF. Also, under dynamic conditions the microballoons are not as uniformly crushed as in static cases. The IPC samples show debonding of aluminum ligaments from the surrounding SF as well.

- Unlike static results, the high-speed optical recordings of the deformation process reveal significant spring-back in SF whereas it is negligible in case of IPC. Also, the failure process is rather uniform in both SF and IPC and no evidence of spatially progressive failure (crushing) is seen at the loading rates of 1500/sec used in this study.

- A unit-cell model of the IPC using a space-filling polyhedron – tetrakaidecahedron or a Kelvin cell was successfully developed using ABAQUS. Infinite elements were also used to model the external surfaces of the unit-cell.

- The stress-strain responses of the model IPC's with 10% - 40% V_f of microballoons in SF were compared to those from experiments. A good agreement between the simulated and the experimental results was observed.

- Contour plots of von-Mises stress, equivalent plastic strain and displacement in the loading direction were analyzed. It was observed that maximum stress concentrations occurred at the vicinity of the aluminum ligament joints and the SF region experienced higher plastic strains than the aluminum region. The proportions of kinetic and strain energies absorbed by aluminum and SF regions were also analyzed.

- Citing the conformance of the results of the unit-cell model to those of the experimental results, the proposed method of finite element analysis could be used effectively to predict the energy absorption characteristics of different material combinations.

REFERENCES

1. Sarikaya M, 'An introduction to biomimetics - A structural view point', *Microscopy research and technique*, 27(5), pp 360-375, 1994.

2. Jhaver R, 'Compression response and modeling of interpenetrating phase composites and foam-filled honeycombs', *MS thesis, Auburn University*, 2009.

3. Clark D. R., 'Interpenetrating phase composites', *Journal of the American Ceramic Society*, 75(4), pp 739-759, 1992.

4. Nammi SK, Myler P, Edwards G, 'Finite element analysis of closed-cell aluminum foam under quasi-static loading', *Materials and design*, 31(2), pp 712-722, 2010.

5. Hopkinson B, 'A Method of Measuring the Pressure Produced in the Detonation of High Explosives or by the Impact of Bullets', *Philosophical Transactions of the Royal Society of London. Series A, Containing Papers of a Mathematical of Physical Character*, 213, 437-456, 1914.

6. Robertson R, 'Some properties of explosives', *Journal of the Chemical Society, Transactions*, 119, 1-29, 1921.

7. Landon JW and Quinney H, 'Experiments with the Hopkinson pressure bar', *Philosophical Transactions of the Royal Society of London. Series A, containing Papers of a Mathematical or Physical Character*, 103, 622-643, 1923.

8. Davies RM, 'A critical study of the Hopkinson pressure bar', *Philosophical Transactions of the Royal Society of London. Series A, Mathematical and Physical Sciences*, 240, 375-457, 1948.

9. Kolsky H, 'An investigation of the mechanical properties of materials at very high rates of strain', *Proceedings of the Physical Society. Section B*, 62, 676-700, 1949.

10. Ramesh KT, Narasimhan S, 'Finite deformations and the dynamic measurement of radial strains in compression Kolsky bar experiments', *International journal of solids and structures*, 33(25), pp 3723-3738, 1996.

11. Frew DJ, Forrestal MJ, Chen W, 'A split Hopkinson pressure bar technique to determine compressive stress-strain data for rock materials', *Experimental mechanics*, 41(1), pp 40-46, 2001.

12. Frew DJ, Forrestal MJ, Chen W, 'Pulse shaping techniques for testing brittle materials with a split Hopkinson pressure bar', *Experimental mechanics*, 42(1), pp 93-106, 2002.

13. Chen W, Zhang B, Forrestal MJ, 'A split Hopkinson bar technique for low-impedance materials', *Experimental mechanics*, 39(2), pp 81-85, 1999.

14. Chen W, Lu F, Zhou B, 'A quartz-crystal-embedded split Hopkinson pressure bar for soft materials', *Experimental mechanics*, 40(1), pp 1-6, 2000.

15. Chen W, Lu F, Frew DJ, et al., 'Dynamic compression testing of soft materials', *Journal of applied mechanics - Transaction of the ASME*, 69(3), pp 214-223, 2002.

16. Song B, Chen W, 'Dynamic compressive response and failure behavior of an epoxy syntactic foam', *Journal of composite materials*, 38(11), pp 915-936, 2004.

17. Subhash G, Liu QL, 'Quasistatic and dynamic crushability of polymeric foams in rigid confinement', *International journal of impact engineering*, 36(10-11), pp 1303-1311, 2009.

18. Bouix R, Viot P, Lataillade JL, 'Polypropylene foam behavior under dynamic loadings: Strain rate, density and microstructure effects', *International journal of impact engineering*, 36(2), pp 329-342, 2009.

19. Prielipp H, Knechtel M, Claussen N, 'Strength and Fracture toughness of aluminum alumina composites with interpenetrating networks', *Materials Science and Engineering A*, 197(1), pp 19-30, 1995.

20. Breslin MC, Ringnalda J, Xu L, 'Processing, microstructure, and properties of co-continuous alumina-aluminum composites', *Materials Science and Engineering A*, 195(1-2), pp 113-119, 1995.

21. Travitzky NA, Gutmanas EY, Claussen N, 'Mechanical properties of Al2O3/Si composites fabricated by pressureless infiltration technique', *Materials letters*, 33(1-2), pp 47-50, 1997.

22. Wegner LD, Gibson LJ, 'The mechanical behavior of interpenetrating phase composites – I: modeling', *International Journal of Mechanical Sciences*, 42(5), pp 925-942, 2000.

23. Wegner LD, Gibson LJ, 'The mechanical behavior of interpenetrating phase composites – I: resin-impregnated porous stainless steel', *International Journal of Mechanical Sciences*, 43(4), pp 1061-1072, 2001.

24. Skirl S, Hoffman M, Bowman K, 'Thermal expansion behavior and macrostrain of Al2O3/Al composites with interpenetrating networks', *Acta Materalia*, 46 (7), pp2493-2499, 1998.

25. Mayer H, Papakyriacou M, ' Fatigue behavior of graphite and interpenetrating graphite-aluminum composite up to 10(9) load', *Carbon*, 44 (9), pp 1801-1807, 2006.

26. Tilbrook MT, Moon R, Hoffman M, 'On the mechanical properties of alumina-epoxy composites with an interpenetrating network structure', *Materials Science and Engineering A*, 393(1-2), pp 170-178, 2005.

27. Etter T, Kuebler J, Frey T, 'Strength and fracture toughness of interpenetrating graphite/aluminium composites produced by the indirect squeeze casting process', *Materials Science and Engineering A*, 386(1-2), pp 61-67, 2004.

28. Jhaver R and Tippur HV, 'Processing, compression response and finite element modeling of syntactic foam based interpenetrating phase composite (IPC)', *Materials Science and Engineering A*, pp 507-517, 2009.

29. Hiel C, Dittman D and Ishai O, 'Composite sandwich construction with syntactic foam core – A practical assessment of post impact damage and residual strength', *Composites*, 24(5), pp 447-450, 1993.

30. Shutov FA, 'Syntactic polymer foams', *Advances in Polymer Science*, 73-4, pp 63-123, 1986.

31. Gupta N, 'A functionally graded syntactic foam material for high energy absorption under compression', *Materials Letters*, 61(4-5), pp 979-982, 2007.

32. Gibson LJ, 'Mechanical Behavior of Metallic Foams', *Annual review of materials science*, 30, pp 191-227, 2000.

33. Malinowski JZ, Klepaczko JR, 'A unified analytic and numerical approach to specimen behavior in the split-Hopkinson pressure bar', *International journal of mechanical sciences*, 28(6), pp 381-391, 1986.

34. Meyers M, 'Dynamic Behavior of Materials', *John Wiley & Sons, Inc.*, pp 305-307, 1994.

35. Mulliken AD and Boyce MC, 'Mechanics of the rate-dependent elastic-plastic deformation of glassy polymers from low to high strain rates', *International Journal of Solids and Structures*, 43, pp 1331-1356, 2006.

36. Kim HS, Plubrai P, 'Manufacturing and failure mechanisms of syntactic foam under compression', *Composites Part A: Applied Science and Manufacturing*, 35(9), pp 1009-1015, 2004.

37. Butcher RJ, Rousseau CE, Tippur HV, 'A Functionally graded particulate composite: Preparation, measurements and failure analysis', *Acta Materialia*, 47(1), pp 259-268, 1998.

38. Gong L, Kyriakides S, Jang WY, 'Compressive response of open-cell foams. Part I: Morphology and elastic properties', *International Journal of Solids and Structures*, 42, pp 1355-1379, 2005.

39. Thompson W (Lord Kelvin), 'On the division of space with minimum partitional area', *Philosophical Mag.*, 24, pp 503-514, 1887.

40. Abaqus analysis user's manual v 6.8.

41. Abaqus theory manual v 6.8.

42. Mendelson S, 'Plasticity: Theory and application', *Robert E. Krieger publishing company*, pp 98-121, 1983. ISBN 0-89874-582-9.

43. Bettess P, 'Infinite elements', *International Journal for numerical methods in engineering*, 11, pp 53-64, 1977.

44. Haggblad B, Nordgren G, 'Modeling non linear soil-structure interaction using interface elements, elastic-plastic soil elements and absorbing infinite elements', *Computers & Structures*, 26, pp 307-324, 1987.

45. Viladkar MN, Godbole PN, Noorzaei J, 'Soil-structure interaction in plane frames using coupled finite-infinite elements', *Computers & Structures*, 39, pp 535-546, 1991.

46. Park WS, Yun CB, Pyun CK, 'Infinite elements for evaluation of hydrodynamic-forces on offshore structures', *Computers & Structures*, 40, pp 837-847, 1991.

47. Zhao CB, Valliappan S, 'A dynamic infinite element for 3-dimensional infinite-domain wave problems', *International journal for numerical methods in engineering*, 36, pp 2567-2580, 1993.

APPENDIX A

The epoxy resin used for preparing SF and IPC foam samples was characterized under both static and dynamic loading conditions. For completeness, the corresponding data is reported in Fig. A1. The quasi-static response of neat epoxy shows three distinct regions: initial linear elastic region, softening region following yielding, and a plateau stress region. A yield stress of approximately 80±2 MPa is followed by a plateau stress of ~ 48 MPa up to 22% true strain. At higher strains (not shown), there is a densification of stress. (The sample continues to densify up to 70% strain).
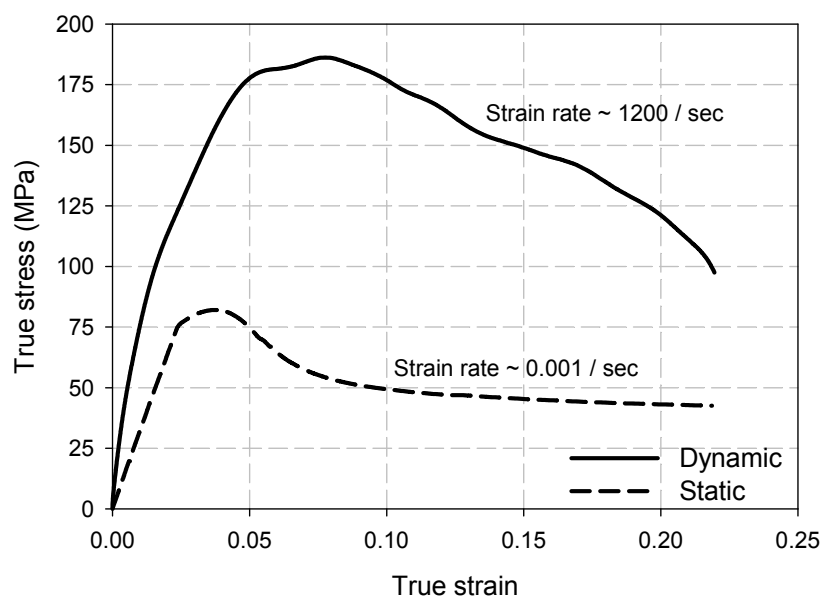

Figure A1: Quasi-static and dynamic compressive responses of neat epoxy

("Epo-Thin") used in SF and IPC foams

The dynamic response, on the other hand, has only two distinct regions. Following an initial linear response with a higher elastic modulus than the quasi-static counterpart, a maximum yield stress of ~185±5 MPa is attained by the neat epoxy sample. Subsequently, the sample shows a monotonic softening response until the stress pulse ends.